YIELD-LINE PLASTICITY AND TENSILE MEMBRANE ACTION IN LIGHTLY-REINFORCED RECTANGULAR CONCRETE SLABS

Ian Burgess

Department of Civil and Structural Engineering, University of Sheffield, Sheffield S1 3JD, United Kingdom
(email: *ian.burgess@sheffield.ac.uk*)

ABSTRACT

The paper provides the systematic derivation of a new analytical approach to tensile membrane action of lightly-reinforced thin concrete slabs at large deflections. The basic motivation for the work comes from the recent use of tensile membrane action as an enhancement, in the fire condition, of the capacity of the thin concrete slabs which are normally made composite with downstand steel beams, at temperatures which have substantially degraded the contribution of these steel beams. The method accepts as a premise that such slabs form a pattern of localized yield lines as an initial small-deflection failure mechanism, and that these yield lines retain their positions as subsequent deflection occurs. As the slab deflects, maintaining the correct kinematics of the articulation and displacement of the system of slab facets, interacting across the yield lines, is extremely important to the horizontal equilibrium of the slab. In this process it becomes necessary to re-think the basic assumption of traditional yield-line theory that any local cross-section of unit width along a yield line equilibrates the force of its concrete compression block with the yielded steel's tension force, producing constant plastic moment capacities for the mesh in either direction along any yield line. In the approach set out in this paper only overall equilibrium of the system of facets needs to be maintained. As in normal rigid-plastic analysis, concrete acts only when compressed, and then at its compressive strength, and steel acts at its tensile yield strength whilst it remains intact. However, steel in either direction can fracture when the local crack-width causes its local strain to exceed its fracture ductility. When the rebar crossing the diagonal yield lines begins to fracture this generally indicates that the slab's capacity is about to reduce with further deflection. The paper does not attempt to address how a rebar's free length across a discrete crack is generated, or the limiting crack widths implied, but this is shown in a range of examples to be a major issue if tensile membrane action is to be used in practice to enhance the capacity of slabs, for example in hazard loading situations. It is important that principles be established in future to quantify this aspect of rebar ductility.

Key Words: *composite slabs, fire, concrete slabs, tensile membrane action, yield line theory*

YIELD-LINE PLASTICITY AND TENSILE MEMBRANE ACTION IN LIGHTLY-REINFORCED RECTANGULAR CONCRETE SLABS

Ian Burgess

1. **INTRODUCTION**

The strength behaviour of concrete slabs, as well as the investigation of calculation methods suitable for routine use in design, generated significant interest during the 1950s and 1960s, following the initial publication in Swedish of yield-line theory by Johansen [1] in 1943; this was later translated into English, but had in any case rapidly been picked-up, explained and developed by others [2, 3]. Johansen's theory concerns the plastic limit-states of reinforced concrete slabs, in principle of any shape, size, support conditions and reinforcement ratio, although in practice being most relevant to under-reinforced slabs. It is postulated that, after undergoing some small elastic displacement the slab develops a pattern of discrete plastic hinges which, when complete, comprise its "failure" mechanism. The development sequence for a simply supported rectangular slab is illustrated in Figure 1.

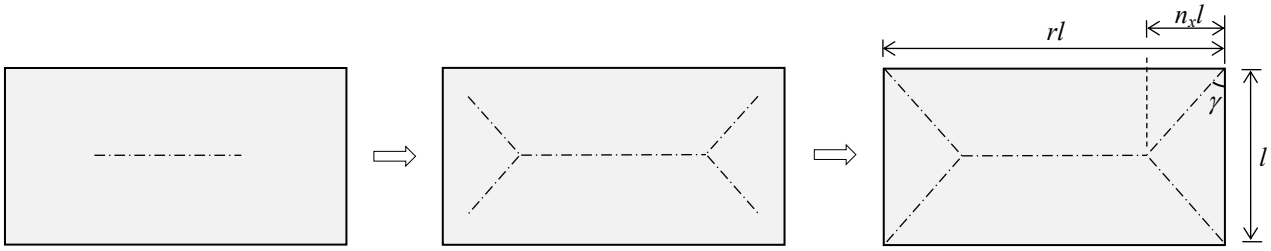

Figure 1: Stages of development of a yield-line mechanism in a concrete slab.

The slab forms flat facets between the linear plastic hinges, known as yield lines, at which relative rotations take place. The load capacity of a given mechanism geometry can be calculated simply by equating the loss of potential of the external loading in deflecting the slab's surface in this way with the plastic work done along the yield lines in articulating to create the deflection. For any assumed mechanism the resulting load capacity prediction lies above or equal to the real limiting capacity; in the case of the rectangular slab shown in Figure 1 the predicted load capacity has to be minimized with respect to the coordinate *nl* of the intersection of the central and diagonal yield lines in order to achieve the exact limiting value. A floor slab may be continuous across many individual edge-supported panels, in which case additional yield lines must be considered just inside the continuous edges.

Tests by Ockleston [4] in the 1950s, on an existing reinforced concrete building, showed load capacities of slabs considerably in excess of those predicted by either yield-line theory or by the simpler Hillerborg [5-7] strip rationalisation. This was later confirmed [8–10] in many academic

research tests. In conventional two-way-spanning reinforced concrete slabs, with flat soffit and moderate span as well as restraint to horizontal edge movement given by adjacent slab panels, the slab depth is usually sufficient for a compressive membrane action (CMA) to account for this apparent strengthening. This effect is actually an arching action which creates a shallow dome-shaped surface of resultant compressive thrust within the thickness of the slab. In slab panels which are thinner relative to their overall dimensions this mechanism may initially occur if the necessary horizontal edge-restraint is present, but will undergo a "snap-through" instability at very low deflection, effectively inverting the thrust surface which then acts as a hydrostatic tensile membrane field. In contrast to compressive membrane action, this tension can be equilibrated internally within the slab panel by a narrow circumferential field of principal compression stress; this is facilitated by concrete's strength in compression. This mechanism is known as tensile membrane action (TMA), which demands only transverse support around all the slab's edges in order to make it work.

The load-carrying mechanism in the horizontal plane, illustrated in Figure 2, is analogous to the force transfer in a bicycle wheel (although without the pre-tension in the spokes), with a radial tension field balanced by circumferential compression. In the transverse direction the external loading within any closed area is largely supported by integration of the vertical components of the same radial tension, at their corresponding inclinations, around its perimeter. In Figure 2 the plan view of a rectangular slab shows simple vertical support provided around its edges.

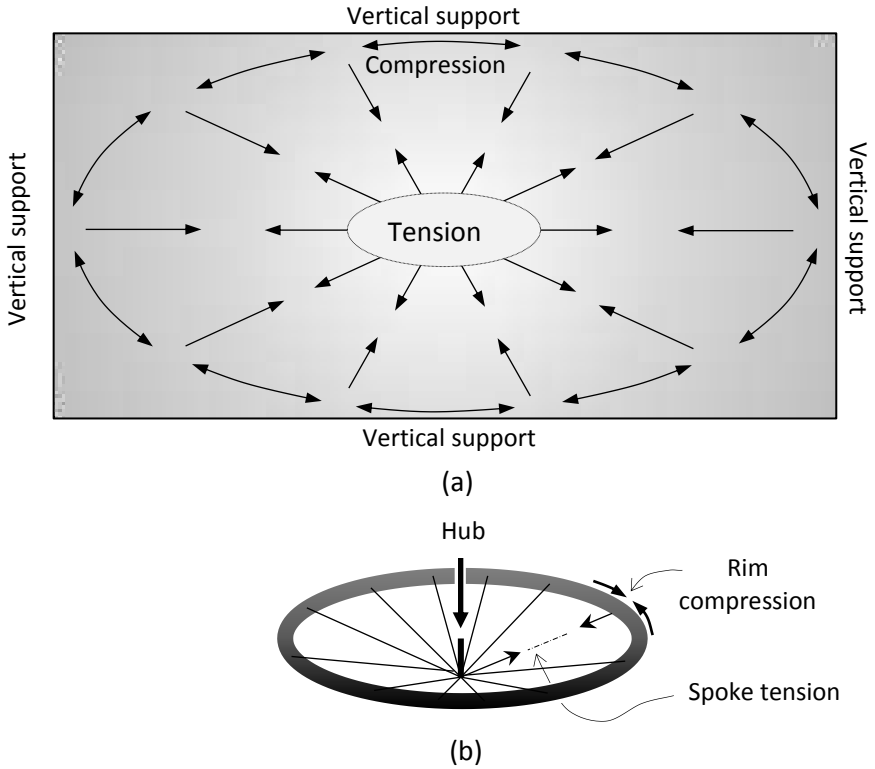

Figure 2: Illustrations of tensile membrane action. (a) Stresses in a concrete slab; (b) Forces in a bicycle wheel.

In practical situations, especially where TMA is used in structural fire engineering calculations for composite floors for which unprotected steel beams within a slab panel area lose nearly all of their strength at high temperatures, the edge support is usually provided by strong edge beams. In the fire case the steel edge beams are protected with insulating material so that they retain a much larger proportion of their strength than the internal beams, but under prolonged heating will eventually achieve very high temperatures and fail to provide the necessary degree of support.

1.1 Historical approaches

Most of the existing analytical research work on TMA took place during the 1960s, the most significant published work being by Sawczuk and Winnicki [11], Kemp [12] specifically on square slabs, and Hayes [13, 14]. At an earlier stage Wood [15] had pointed out a frequent observation from tests to failure of concrete slabs that, while rotational hinges formed in the regions of the yield lines, generally in accordance with yield-line theory, a purely tensile crack also formed at high deflections across the shorter span of the slab. This crack caused by membrane tension is located most usually at the middle of the longer span, but either one or two are sometimes observed as originating at the intersection of the central and diagonal yield lines. The small-deflection yield-line mechanism and the two alternative large-deflection failure mechanisms are shown in Figure 3. Because of the brittle nature of concrete in tension, and particularly for lightly-reinforced slabs for which the yield lines are highly localised, it is logical that as deflections increase these yield lines do not change their locations but their hinge articulations increase.

Sawczuk and Winnicki [11] developed analytical models for all three of these situations, assuming that large deflections are caused simply by relative rotations at the yield lines together with stretching of reinforcement across yield lines and at any tension cracks, as dictated by the kinematics of the particular case under consideration. Their set-up of the basic case, shown in Figure 3(a), allows rotation about, but no movement of the mid-surface across, all the edges of the panel.

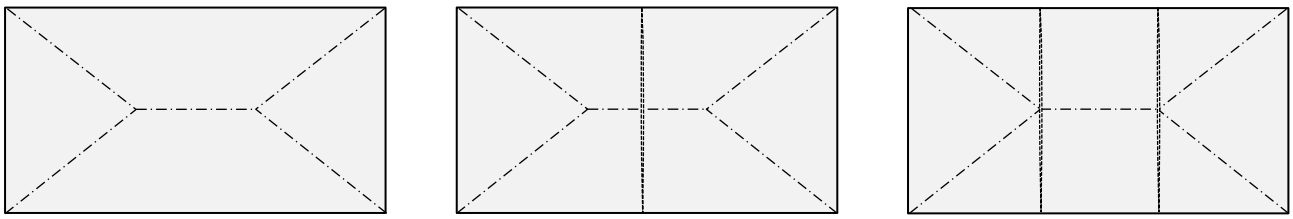

(a) Small- or large-deflection yield line mechanism.

(b) Large-deflection yield-line mechanism including a central tensile crack.

(c) Large-deflection yield-line mechanism including cracks at yield-line intersections.

Figure 3: Different plastic mechanisms considered by Sawczuk and Winnicki [9].

For the other cases the corners of the panel are prohibited from moving, although rotations of the slab facets are allowed about these points. Their analysis is based on an approximation of the interaction curve between moment capacity and membrane force at an isolated (beam) cross-section assuming a rectangular concrete compression stress block. For the basic case, and depending on the deflection magnitude, they postulate that a diagonal yield line can contain up to three distinct zones: a zone adjacent to the slab corner where only bending moments contribute internal work; a zone in which both moment and membrane force do work; finally there may be a zone adjacent to the yield-line intersection where only membrane force does work. The latter corresponds to the length of yield line in which there is no concrete stress block, which is particularly relevant at high deflections. The mechanisms in which tensile through-depth cracks have formed are not considered in this paper, although the conditions for their initiation will be discussed at a later stage.

Kemp [12] created a large-deflection yield-line model for the bisymmetric case of square simply supported, isotropically reinforced slabs under uniformly distributed loading, as a more practically relevant development from Wood's [15] solution for a circular slab. Kemp's method uses a kinematically admissible extension of the classic diagonal yield-line mechanism for infinitesimal deflections which allows compatible movement of the edges of the slab as well as their rotation, in order to generate in-plane equilibrium of the four triangular slab facets, taking account of the movement of the neutral axis which delimits the concrete stress block along a yield line. This allows the yield lines to separate completely at some value of the deflection, giving a central zone of pure tension which grows in width as the deflection increases. This will be seen to resemble strongly the method which is introduced in this paper for rectangular slabs, although Kemp uses an equilibrium method, taking moments about the slab edges, rather than by equating the internal work with the loss of potential of the external load which is used to calculate the yield-line initial failure load.

Hayes [13, 14] developed a different equilibrium method, addressing rectangular slabs with orthotropic reinforcement. He initially extended Sawczuk's solution to the case of rectangular orthotropically-reinforced slabs, whilst accepting that the method implied the existence of boundary constraint forces which would not exist around simply supported slabs, and that its predictions for the case of square slabs varied considerably from Kemp's. However his main development was of a new equilibrium method to calculate the enhancement of load capacity for rectangular slabs with orthotropic reinforcement. The method is once again based on the optimal small-deflection yield-line mechanism with moderate deflections imposed upon it. He assumed two alternative membrane force distributions; a linearly-varying distribution of net membrane force along the diagonal yield lines (Figure 4(a)), and a similar distribution from the corners of the slab which then becomes

constant (Figure 4(b)) when the yield lines separate over the whole slab depth in the vicinity of the yield-line intersection.

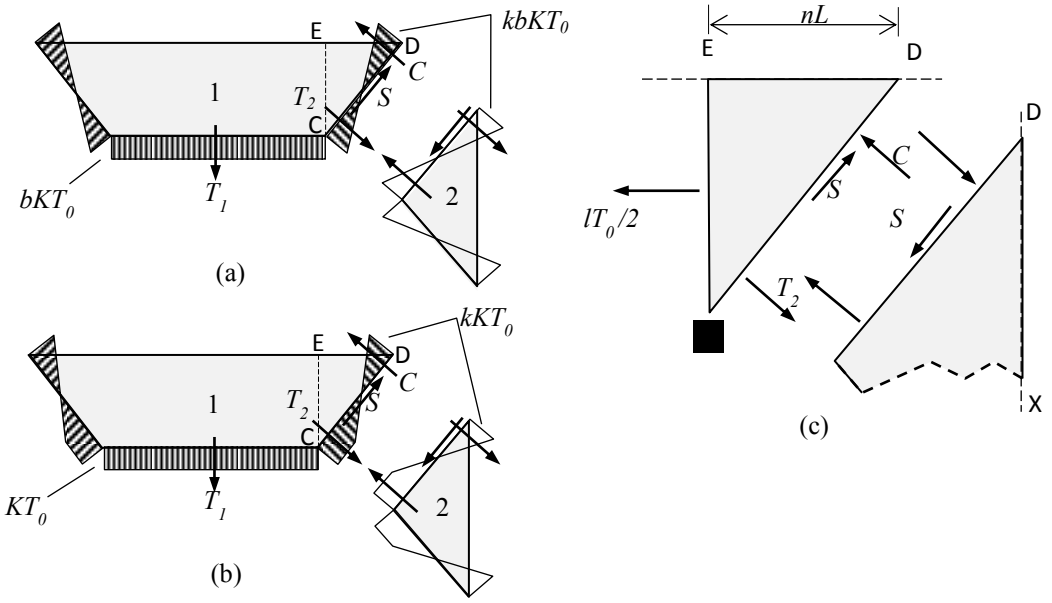

Figure 4: Hayes's [10, 11] membrane force models. (a) Concrete contact on whole length of diagonal yield lines; (b) No concrete contact near yield line intersections; (c) In-plane equilibrium of forces.

In these figures the notations T_0 and KT_0 represent the yield strengths per unit slab width of the mesh aligned in the *x*- and *y*- directions respectively. Hence it is hard to see why there is an assumed commonality of membrane force between the longitudinal and diagonal yield lines at their intersection (the point C) in both cases.

It must be pointed out that these are simply treated as two alternative assumptions. Since there is no attempt to make the slab's movements and rotations compatible with the membrane force distributions, the first assumption cannot predict the critical deflection at which contact ceases between the yield-line crack faces at the intersection, beyond which the second assumption would be more logical. Hayes makes the assumption that the "failure" condition is when the through-depth tension crack has formed from the yield-line intersection, as shown in Figures 3(c) and 4(c), and uses in-plane equilibrium of the forces on the sides of the triangles ECD, together with in-plane equilibrium of Facets 1 and 2, to determine the exact values of *k* and *b*, which define the membrane force distributions. Then, by taking the moments about the slab edges ED (for Facet 1) and DX (for Facet 2), the load capacities of each of the facets at any deflection, due only to the membrane forces and their lever arms about the edges, are found. These are expressed as "enhancements" e_{1m} and e_{2m} relative to the small-deflection yield-line load capacity. The load capacities of the facets due to

the plastic bending moments distributed along the yield lines, amended by the presence of the coincident membrane forces, are not included in these calculations but are then aggregated as separate "enhancements" e_{1b} and e_{2b}, again relative to the small-deflection capacity. The membrane and bending moment enhancement factors for each facet are added together, to produce separate overall enhancement factors $e_1 = e_{1m} + e_{1b}$ and $e_2 = e_{2m} + e_{2b}$ for the two facets. These enhancement factors are generally unequal. This is because the resultant vertical shear forces on the diagonal yield lines are not included in the moment calculations. In their absence a weighted average enhancement factor is given (without proof) as

$$e = e_1 - [\frac{(e_1 - e_2)}{(1 + 2\mu\alpha^2)}] \quad (1)$$

in which μ is the coefficient of orthotropy and α is the slab aspect ratio.

It is worth mentioning here that, in unpublished work, Gillies [16] has included the vertical shear resultants with the membrane forces in the first moment equations, eliminated these between the two facets, and calculated a single enhancement factor

$$e = e_1 - [\frac{(e_1 - e_2)}{(1 + 2n\mu\alpha^2)}] \quad (2)$$

in which n is the proportion of the longer span which locates the position of the yield-line intersection point, as shown in Fig. 4, and e_1 and e_2 are defined as above.

1.2 Recent developments

Interest in the subject of TMA appears to have lapsed after publication of these initial studies; large deflections are unacceptable in terms of normal building serviceability, and so the subject was seen as of being only of academic interest. A relevant application became apparent in the late 1990s, in the context of composite construction, particularly for composite floors composed of thin, very lightly-reinforced concrete slabs acting compositely with an array of parallel downstand steel beams. When combined with profiled steel decking through which shear studs are welded onto the upper flanges of the downstand beams, this system of constructing floors is quick to construct and very economical; its major perceived disadvantage is that traditional fire resistance design usually requires all the steel beams to be fire-protected. This process can add a considerable percentage to the frame cost, and can also cause extended construction times if performed on-site. A series of monitored fire tests was carried out [17] in 1995-96 at Cardington, in different parts of a loaded full-scale 8-storey building constructed using steel columns and composite floors. In all these tests the columns were protected, but steel downstand beams were overwhelmingly left unprotected. In

simple terms the most notable statistic from the test series was that, whereas existing codes of practice, such as BS5950 Part 8 [18] and the pre-standard ENV1994 Part 1-2 [19], predicted that all composite beams should have failed at a steel cross-section temperature of about 680°C, in almost every test the steel temperature considerably exceeded this value without any structural failure occurring. It was quickly recognized [20, 21] that this reserve of strength in the composite system, when the steel beams had lost most of their strength, must be due to TMA in the concrete slabs which formed part of the composite floor. It was notable that slab deflections were very large in all the tests, and that curvatures were distinctly biaxial; these are the essential conditions for TMA to occur. In the aftermath of the Cardington tests a design method based on the enhancement of yield-line capacity in composite slabs with unprotected downstand beams supported by protected edge-beams was developed by Bailey [22-25] at the Building Research Establishment. This method has been used in structural fire engineering design in the UK from the year 2000 up to the present. Its model of TMA is also the basis of the New Zealand Slab Panel Method by Clifton [26], and it has recently been adopted almost in its entirety by design guidance documents [27, 28] emanating from the European research programme FRACOF.

Bailey's model is very much based on the work of Hayes, using identical assumptions on the force distributions along all of the yield lines, but apparently ignores the case shown in Figure 4(b) in which through-depth cracks are generated from the yield-line intersections, gradually spreading towards the slab corners as the deflection increases. Hence, the distribution of membrane force along these yield lines is always linear in this model. However, Bailey uses the more common observation from tests, which is that the eventual through-depth tension crack tends to occur across the middle of the longer dimension of the slab (Figure 3(b)) rather than at the yield-line intersections. Hence his force system for in-plane equilibrium is as shown in Figure 5, on the edges of a semi-trapezoidal quadrilateral, rather than a triangular, slab facet.

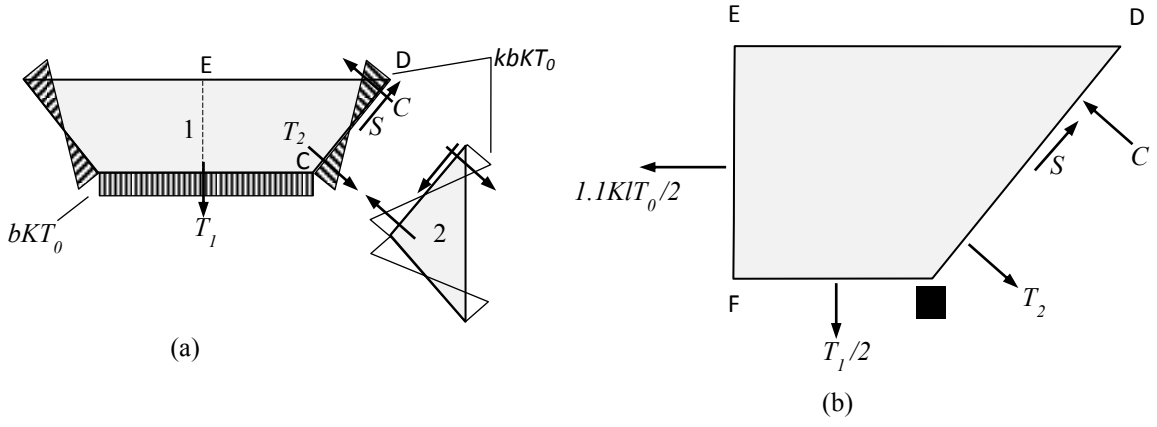

Figure 5: Bailey's [10, 11] membrane force model. (a) Concrete contact on whole length of diagonal yield lines; (b) In-plane equilibrium of forces.

The in-plane equilibrium of the assumed forces shown in Figure 5(b) is addressed in similar fashion to Hayes, by resolving in two directions and taking moments about the point E. Bailey departs from Hayes's assumption that the reinforcement crossing the through-depth crack is at its yield strength, by assuming an ultimate strength which is 10% higher. Beyond this, the enhancement factors e_1 and e_2 are found for each of the facets by taking moments about the supported edges, and a single weighted average enhancement factor is once again calculated using Equation (1).

Bailey's method is, of course, mainly aimed at TMA in composite floors in fire, and adds the enhanced capacity of the slab at any deflection to the reduced capacity of the unprotected composite beams due to elevated temperature. It then applies a deflection limit to the TMA, which attempts to represent a safety-factored version of that at which the reinforcement across the through-depth crack fractures. This deflection limit is itself questionable, but since it applies only to the high-temperature case it will be dealt with in a subsequent paper. The present paper presents a more complete approach to the basic mechanics of TMA of lightly-reinforced rectangular concrete slabs than those postulated previously, and is not at this stage of its development concerned with the effects of elevated temperatures. However, the ultimate aim of the work is very definitely to develop a kinematically-consistent process to gauge the enhancement of failure temperatures for composite floor panels in fire conditions.

An aspect of small-deflection yield-line mechanisms which tends to be neglected is that, as the ratio of reinforcement strengths per unit width (f_{px} and f_{py}) in the *x*- and *y*-directions changes, the geometry of the optimal yield-line mechanism also changes. As is illustrated in Figure 6(a), isotropic mesh (with $\Omega = f_{px} / f_{py} = 1$) and lower values of Ω produce optimum mechanisms with their central yield-lines aligned in the longer-span (*x*) direction, and the value of the intersection coordinate n_x increases as Ω increases.

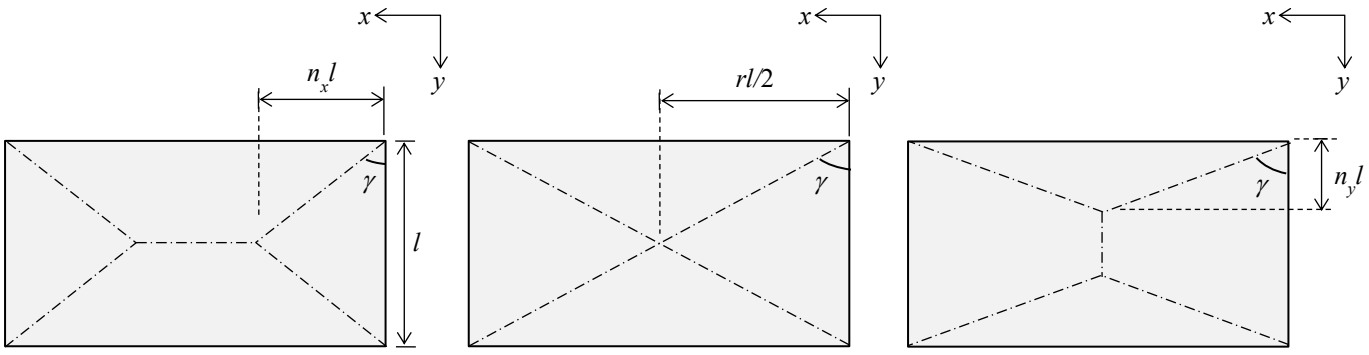

(a) Low f_{px}/f_{py}, including 1.0 (b) Transition f_{px}/f_{py} (c) High f_{px}/f_{py}

Figure 6: Changes in yield-line geometry for different ratios f_{px}/f_{py}. (a) x-aligned; (b) transition; (c) y-aligned.

At some value of $\Omega > 1$ the intersection coordinate reaches the centre of the slab ($n_x = r/2$), the transition state shown in Figure 6(b). For even higher values of Ω the central yield line is aligned in the *y*-direction (Figure 6(c)) and the intersection coordinate n_y decreases progressively as Ω increases. The issue of calculating the alignment of the mechanism, and the optimal value of n_x or n_y will be considered later. The process for finding the enhancement of yield-line capacity due to TMA will be defined in detail for the *x*-aligned mechanism, and the results for the *y*-aligned mechanism will then be presented.

2. MECHANICS OF DEFLECTION OF YIELD-LINES

The redeveloped analysis of rectangular slabs is based on the three essential principles of plastic theory; kinematics, equilibrium and plastic material properties. It is assumed that, for a slab under uniformly distributed transverse loading, a pattern of yield lines forms at some value of load intensity. If the loading is increased beyond this "failure" value, the geometry of the yield-line pattern is fixed and cannot change although the deflection increases. Since concrete is a brittle material, when the reinforcement is relatively light cracks tend to be discrete rather than distributed, and once a crack has formed the moment capacity across the crack is lower than that of adjacent zones of the slab, and so there is no inducement for the position of a yield line to change once it has formed. For rectangular slabs the optimal yield lines tend to separate the slab into triangular and trapezoidal flat facets, as discussed earlier.

2.1 The x-aligned mechanism

2.1.1 Kinematics of yield-line deflection

When the optimal yield-line mechanism is deflected by a finite amount δ_A at the intersection of yield lines, which is compatible at the yield-line intersection, the facets interact in a way which is dictated by their shapes, their compatible angles of rotation θ and ϕ, and the rigid-body movements Δ_x and Δ_y of their upper-surface corners. These are shown in Figure 7.

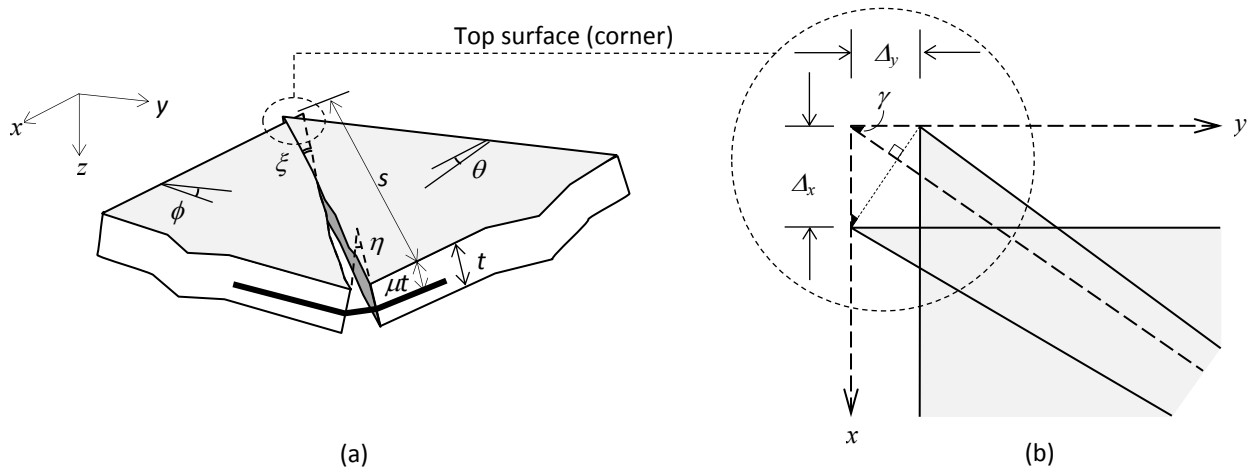

Figure 7: Geometry of diagonal yield-line crack opening. (a) Crack opening at rebar level; (b) Top surface of slab, including rigid-body movements of triangular and trapezoidal slab facets.

The angle of the triangular facet at the slab corner is denoted as γ. If the intersection is located at $n_x l$ in the *x*-direction, as shown in Figure 1, then $\tan\gamma = 2n_x$. The angles of rotation of the facets about their supported edges are related by:

$$\delta_A = n_x l\theta = \frac{l\phi}{2}, \text{ or } \phi = 2n_x\theta = \theta\tan\gamma \tag{3}$$

It is assumed that there is no slip between the facets along the diagonal yield lines. This gives a basic geometric relationship between the rigid-body movements at the top corner, based on the geometry shown in Figure 7(b):

$$\Delta_x \sin\gamma = \Delta_y \cos\gamma \tag{4}$$

Considering moderate finite rotations θ and ϕ of the triangular and trapezoidal facets, and the views onto their crack-faces shown in Figure 8(b) and 8(c), the motions u and v of a point at a certain depth z and coordinates x and y, which is initially common to the facets at zero deflection, in the *x*- and *y*-directions respectively are:

$$u = \Delta_x - \theta z - \frac{\theta^2 x}{2} \tag{5}$$

$$v = \Delta_y - \phi z - \frac{\phi^2 y}{2} \tag{6}$$

or, substituting Equations (1) and (3) into Equation (6):

$$v = u\tan\gamma = 2n_x u \tag{7}$$

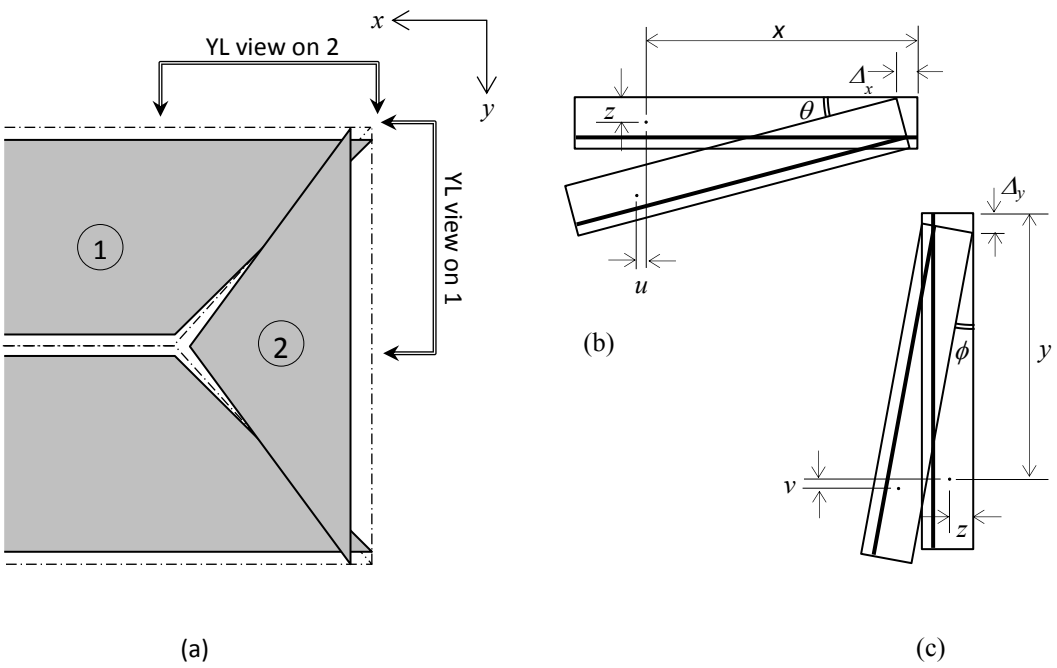

Figure 8: Movements of a point on the diagonal yield line. (a) Plan view of top surface of slab; (b) x-direction motion u on triangular Facet 2; (c) y-direction motion v on trapezoidal Facet 1.

Note that any position on the yield line crack-faces of Facet 1 has $u = 0$ and any position on the crack-faces of Facet 2 has $v = 0$. At any deflection, and given a value of the top corner movement Δ_x, the equation of the neutral axis on each diagonal yield line is therefore given by setting $u = 0$ in Equation (5), or $v = 0$ in Equation (6), to indicate the position at which the facets cease to intersect. The general form is a straight line:

$$z = \frac{\Delta_x}{\theta} - \frac{\theta x}{2} \tag{8}$$

Referring to Figure 9 it can be seen that there are three possible configurations for the concrete stress block.

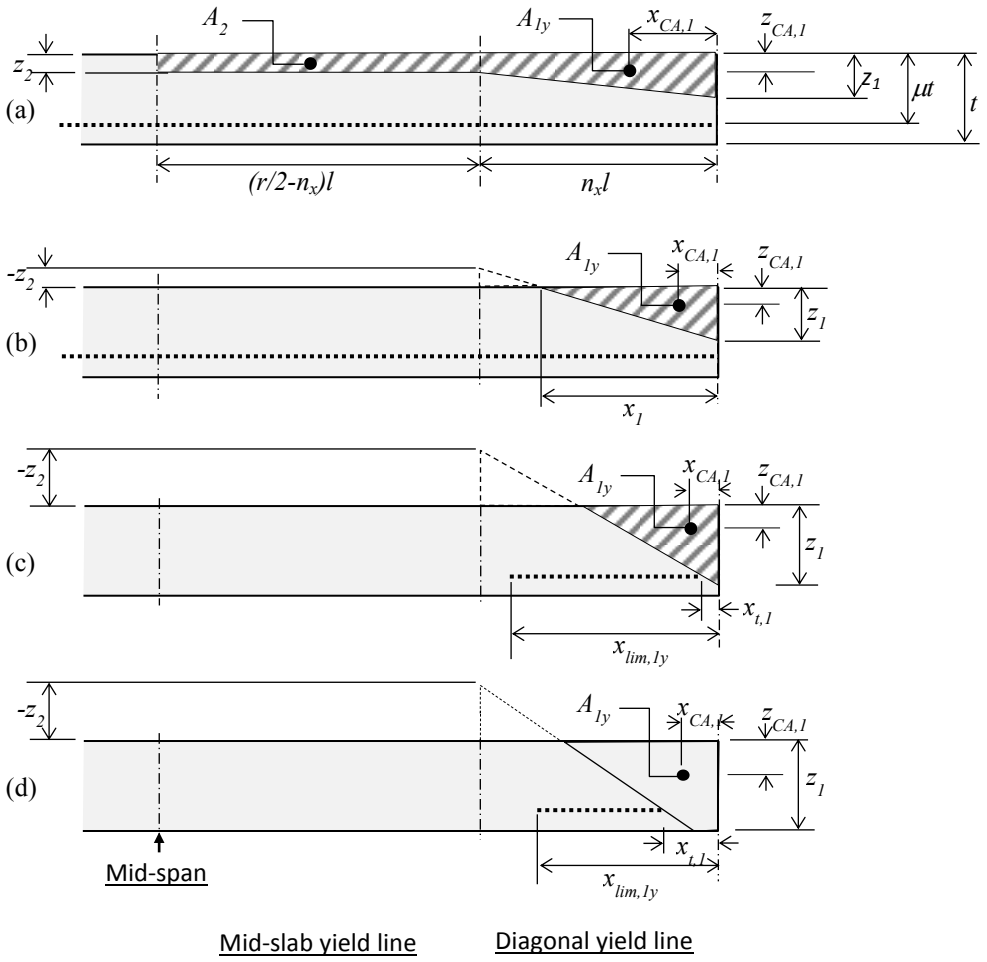

Figure 9: Projection on the x-direction of the yield lines at different stages; (a) Concrete stress blocks on all yield lines; (b) Triangular stress blocks above rebar on diagonal yield lines; (c) Triangular stress blocks below rebar on diagonal yield lines; (d) Trapezoidal stress blocks on diagonal yield lines.

At small deflections (Figure 9(a)) the concrete is compressed on both the central and diagonal yield lines; the stress block is clearly rectangular on the central yield line, but increases its depth towards the slab corners on the diagonal yield lines. At some deflection the central stress block disappears and this yield line has complete separation of the concrete crack-faces, although *y*-direction rebar may still bridge this crack. From this point onwards the stress block on the diagonal yield lines becomes triangular, as shown in Figures 9(b) and 9(c). There is also the possibility that this triangular stress block may go below the lower surface of the slab and become trapezoidal, as seen in Figure 9(d). These configurations may be characterized by the coordinates z_1 and z_2 given by Equation (8), at the slab corner and at the yield-line intersection respectively. In Figures 9(a) and 9(b) the value of z_1 lies below μt, which is the rebar depth, and in Figures 9(c) and 9(d) it lies below

the rebar. On the other hand z_2 is positive in Figure 9(a), and negative in all other cases. From Equation (8) these key coordinates are:

$$z_1 = \frac{\Delta_x}{\theta} \tag{9}$$

and

$$z_2 = \frac{\Delta_x}{\theta} - \frac{\theta n_x l}{2} \tag{10}$$

2.1.2 Solution process

All the forces in the horizontal plane which can cross the yield lines are shown in Figure 10. These are not resultant membrane forces, but the resultant tension forces due to *x*- and *y*-direction rebar acting at yield, and the resultant compression forces from the concrete stress blocks which are assumed to be subject to the compressive strength of the concrete. There is no attempt here to reduce the stress block depth, as tends to be done in current design codes, to take account of the curvilinear growth of concrete stress near to the neutral axis; this can easily be done in developing design guidance from this analysis at a later stage.

Horizontal equilibrium can be established by resolving the *x*-direction forces on the triangular Facet 2 and the *y*-direction forces on the trapezoidal Facet 1. The equilibrium equations are given by:

$$T_{x1} = C\cos\gamma + S\sin\gamma \tag{11}$$

and

$$T_{y1} + T_{y2} = C\sin\gamma - S\cos\gamma + C_{y2} \tag{12}$$

Eliminating *S* from Equations (11) and (12) gives:

$$T_{x1}\cos\gamma + \left(T_{y1} + T_{y2}\right)\sin\gamma = C + C_{y2}\sin\gamma \tag{13}$$

It is assumed that the steel rebar is ineffective where it lies in the compressed zone above the neutral axis, and that *x*- and *y*-direction reinforcement fractures completely at crack openings $\Delta_{lim,x}$ and $\Delta_{lim,y}$, which are defined by its own fracture strain (ductility) and by its bond characteristics with the surrounding concrete. In the simplest terms, it may be assumed that there is zero bond between the positive anchor points either side of a yield line which are created by the welds to the orthogonal bars; the limiting crack opening at the rebar level is then given by the distance between these anchor points for the appropriate bar-direction multiplied by the fracture strain. This is clearly an extreme case, and the crack openings at which fracture takes place will be lower because of the

bond between steel and concrete. However the ductility of the rebar can simply be scaled-down within the zero-bond assumption to represent particular bond assumptions or pull-out test data. The coordinates which limit the distances over which bars deform plastically in tension across yield lines can be defined from the limiting fracture crack-width at the level of the mesh together with Equations (5) and (6), and from the neutral axis definition in Equation (8).

(a) For reinforcement in the *x*-direction the limiting coordinate for fracture is:

$$y_{lim,1x} = \frac{1}{n_x \theta}\left(z_1 + \frac{\Delta_{lim,x}}{\theta} - \mu t \right) \tag{14}$$

up to a maximum value of $l/2$.

At high deflection it is possible for all the *x*-direction reinforcement to fracture. This is the case for $y_{lim,1x} \le 0$, or:

$$z_1 \ge \left(\mu t - \frac{\Delta_{lim,x}}{\theta} \right) \tag{15}$$

If the stress block lies below the mesh level at the slab corner then the limiting coordinate at which mesh is no longer in tension is:

$$y_{t,1} = \frac{1}{n_x \theta}\left(z_1 - \mu t \right) \tag{16}$$

If the stress block lies above the mesh level then $y_{t,1} = 0$.

(b) For reinforcement in the *y*-direction crossing a diagonal yield line the limiting coordinate is:

$$x_{lim,1y} = \frac{2}{\theta}\left(z_1 + \frac{\Delta_{lim,y}}{2\theta n_x} - \mu t \right) \tag{17}$$

up to a maximum value of $n_x l$.

If the stress block lies below the mesh level at the slab corner then the limiting coordinate at which it is no longer in tension is:

$$x_{t,1} = \frac{2}{\theta}\left(z_1 - \mu t \right) \tag{18}$$

If the stress block lies above the mesh level then $x_{t,1} = 0$

(c) For the y-direction reinforcement crossing the central yield line, either all the reinforcement is active, or it has completely fractured when

$$n_x l < \frac{2}{\theta}\left(z_1 + \frac{\Delta_{lim,y}}{4\theta n_x} - \mu t \right) \tag{19}$$

If the strengths per unit width (perpendicular to the bar direction) of the reinforcement in the *x*- and *y*-directions respectively are f_{px} and f_{py}, the concrete compression strength is f_c, and the areas of the concrete stress blocks on the yield lines are A_1 and A_{2y}, the individual force components shown in Figure 10 are given by:

$$C = A_1 f_c \tag{20}$$

$$C_{y2} = A_{2y} f_c \quad \text{or } C_{y2} = 0 \tag{21}$$

$$T_{y1} = \left(x_{lim,1y} - x_{t,1} \right) f_{py} \tag{22}$$

$$T_{x1} = \left(y_{lim,1x} - y_{t,1} \right) f_{px} \tag{23}$$

$$T_{y2} = \left(r/2 - n_x \right) l f_{py} \quad \text{or } T_{y2} = 0 \tag{24}$$

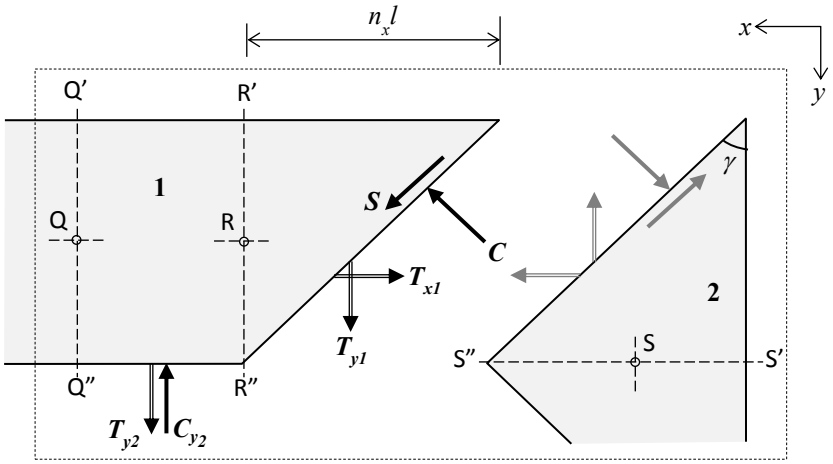

Figure 10: The horizontal force system between facets along the yield lines, for x-aligned mechanisms.

The stages in the solution process are then as follows for any given value of deflection (most conveniently expressed as the rotation θ of Facet 2):

- For any assumed case the expressions for the in-plane forces, given by Equations (20)-(24), are substituted into the equilibrium Equation (13), with the appropriate assumptions for each assumed case, and this is then solved for the value of the only unknown quantity, z_1.
- The assumptions about

- the state of the concrete stress block,
- the state of fracture of the mesh,

are then checked for consistency for all cases assumed using this value of z_1. Only one set of assumptions will be verified.

- For the verified case the plastic internal work done on the central and the four diagonal yield lines is now aggregated on the basis of the quarter-model shown in Figure 10 for the deflection defined by the rotation θ of the triangular facet, as the sum of the multiples of the forces and their appropriate movements for each force component, including both (tensile resultant forces x their crack-face separations) and (compressive resultant forces x their crack-face intrusions). The appropriate movements are those of the centroids of the concrete stress blocks A_1 and A_{2y} and of the resultant bar forces T_{x1}, T_{y1} and T_{y2}. These movements are denoted as $u_C, v_C, v_{C_{y2}}, u_{T_{x1}}, v_{T_{y1}}$ and $v_{T_{y2}}$, and are calculated from Equations (5) and (6) using the coordinates of the appropriate resultant forces. Of these displacements $u_C, u_{T_{x1}}$ are given by movement of the triangular facet, and $v_C, v_{C_{y2}}, v_{T_{y1}}$ and $v_{T_{y2}}$ are given by movement of one half of one trapezoidal facet. In general terms these movements are:

$$u_C = \Delta x - \theta z_{CA,1} - \frac{\theta^2}{2} x_{CA,1} \tag{25}$$

$$v_C = \Delta y - \phi z_{CA,1} - \frac{\phi^2}{2} y_{CA,1} \tag{26}$$

$$v_{C_{y2}} = \Delta y - \frac{\phi}{2} z_2 - \frac{\phi^2}{4} l \tag{27}$$

$$u_{T_{x1}} = \Delta x - \theta\mu t - \frac{\theta^2}{4}\left(x_{Lim,1} + x_{T,1}\right) \tag{28}$$

$$v_{T_{y1}} = \Delta y - \phi\mu t - \frac{\phi^2}{4}\left(\left(y_{Lim,1} + y_{T,1}\right)\right) \tag{29}$$

$$v_{T_{y2}} = \Delta y - \phi\mu t - \frac{\phi^2 l}{4} \tag{30}$$

The expression for loss of potential of the external uniformly distributed load p, which is the same for all cases, is:

$$W_e = pl^3\left(\frac{r}{2}-\frac{n_x}{3}\right)\theta n_x \tag{31}$$

This is equated to the aggregate internal work:

$$W_i = -4\left(T_{x1}u_{T_{x1}} + T_{y1}v_{T_{y1}} + T_{y2}v_{T_{y2}} + C(u_C\cos\gamma + v_C\sin\gamma) + C_{y2}v_{C_{y2}}\right) \tag{32}$$

to give the enhanced load capacity:

$$p = \frac{6W_i}{l^3\theta\left(3r-2n_x\right)n_x} \tag{33}$$

for the assumed value of θ.

2.1.3 Application to particular cases as deflection increases

A total of 30 combinations of the different stress-block configurations (complete and triangular, above and below the mesh; trapezoidal) and reinforcement failure conditions (central yield line intact or fractured; *x*- or *y*-bars, or both, partially fractured) is possible; these combinations are defined in Table 1.

Compression block		Reinforcement mesh fracturing					
		None	Central y (all)	Diagonal x	Central y + diagonal x	Central y + diagonal y	Diagonal x and y
Full	above mesh	**a1x**	**a1x'**	**a1x***	**a1x'***	**a1x****	**a1x*****
	below mesh	**a2x**	**a2x'**	**a2x***	**a2x'***	**a2x****	**a2x*****
Triangular	above mesh	**b1x**	**b1x'**	**b1x***	**b1x'***	**b1x****	**b1x*****
	below mesh	**b2x**	**b2x'**	**b2x***	**b2x'***	**b2x****	**b2x*****
Trapezoidal		**cx**	**cx'**	**cx***	**cx'***	**cx****	**cx*****

Table 1: Combinations of compression block configuration and rebar fracture for x-aligned cases.

For the initial yield-line failure, at minimal deflection, the case is **a1x**, for which all the reinforcement is intact and lies below the complete stress blocks. As the deflection is increased, the key dimensions which define the stress blocks change; z_1 increases and z_2 decreases, as the crack width at the mesh level increases. There are therefore several possibilities for the subsequent case, depending on which of the following happens first:

- z_2 becomes negative; Case **b1x**.
- The central rebar fractures; Case **a1x'**.
- z_1 exceeds μt; Case **a2x**.

Beyond this first change of case the scope for further changes expands considerably

2.1.4 Initial increase of deflection: Case a1

A general section showing the surfaces of the first yield-line mechanism with stress blocks on all yield lines and all rebar intact, viewed as a projection into the *x*-direction, is shown in Figure 9(a). It is worth showing the calculation process for this case in detail.

The equations of the neutral axes are:

$$z = z_1 - \frac{\theta x}{2} \tag{34}$$

on the diagonal yield line, and $z = z_2 = z_1 - \frac{\theta n_x l}{2}$ on the central yield line. The concrete stress block areas are:

$$A_{1y} = \frac{n_x l}{2}\left(z_1 + z_2\right) = \frac{n_x l}{2}\left(2z_1 - \frac{\theta n_x l}{2}\right) = A_1 \sin\gamma \tag{35}$$

$$A_{2y} = l\left(\frac{r}{2} - n_x\right) z_2 = l\left(\frac{r}{2} - n_x\right)\left(z_1 - \frac{\theta n_x l}{2}\right) \tag{36}$$

The concrete compression forces are therefore:

$$C = \frac{f_c n_x l}{\sin\gamma}\left(z_1 - \frac{\theta n_x l}{4}\right) \tag{37}$$

$$C_{y2} = f_c l\left(\frac{r}{2} - n_x\right)\left(z_1 - \frac{\theta n_x l}{2}\right) \tag{38}$$

The steel forces in plastic tension are:

$$T_{y1} = f_{py} n_x l \tag{39}$$

$$T_{x1} = f_{px}\frac{l}{2} \tag{40}$$

$$T_{y2} = f_{py} l\left(r/2 - n_x\right) \tag{41}$$

It is convenient at this stage to use dimensionless versions of various defining parameters:

$$\lambda_x = \frac{f_{px}}{f_c l} \quad \text{and} \quad \lambda_y = \frac{f_{py}}{f_c l} \tag{42}$$

$$\psi_1 = \frac{z_1}{l} \quad \text{and} \quad \psi_2 = \frac{z_2}{l} = \psi_1 - \frac{\theta n_x}{2} \tag{43}$$

$$\tau = \frac{t}{l} \tag{44}$$

For future reference, outside this case, the limiting crack-widths at which mesh fractures are also normalized at this stage as:

$$\eta_x = \frac{\Delta_{lim,x}}{l} \quad \text{and} \quad \eta_y = \frac{\Delta_{lim,y}}{l} \tag{45}$$

Substitution of some of these relationships, with Equations (37)-(41), into Equation (13) gives an equilibrium condition:

$$\psi_1\left(\frac{1}{\sin\gamma\cos\gamma}+\left(r-2n_x\right)\right)-\left(\lambda_x\frac{1}{2n_x}+\lambda_y r\right)-\frac{\theta n_x}{2}\left(\frac{1}{2sin\gamma\cos\gamma}+\left(r-2n_x\right)\right)=0 \tag{46}$$

For any known value of γ (and n_x), ψ_1 is evaluated from this equation. If this is converted back to z_1 and z_2, the concrete forces at the centroids of the areas A_{1y} and A_{2y}, given by Equations (35) and (36), can then be evaluated. For Case **a1** the coordinates of the centroid of the stress block on a diagonal yield line are given from the geometry shown in Figure 8(a) as:

$$x_{CA,1} = \frac{n_x l\left(z_1+2z_2\right)}{3\left(z_1+z_2\right)} \tag{47}$$

$$y_{CA,1} = \frac{x_{CA,1}}{2n_x} \tag{48}$$

$$z_{CA,1} = \frac{\left(z_1^2+z_1z_2+z_2^2\right)}{3\left(z_1+z_2\right)} \tag{49}$$

The plastic work done internally, for any deflection defined by the rotation θ of the triangular facet, and consequently the enhanced load capacity, can now be calculated as in Equations (32) and (33).

2.1.5 Geometry of the yield-line mechanism

The geometry of the yield-line mechanism is determined only once for lightly-reinforced slabs. The pattern which gives the lowest plastic "failure" load intensity p_0 causes discrete cracks which retain their positions during subsequent deflection. In the conventional analytical process, in which it is assumed that the neutral axis depths with respect to the *x*- and *y*-aligned reinforcement can be calculated independently, the optimal mechanism geometry is obtained analytically, by setting the first derivative of the algebraic expression for p_0 with respect to n_x equal to zero. In this case, in which the neutral axis depth is found from the in-plane equilibrium conditions, although an algebraic

expression can be written for p_0, this is sufficiently complex that finding an analytical solution for n_x is difficult unless $\lambda_x = \lambda_y$.

It is relatively straightforward to find the optimum yield-line pattern for a particular case iteratively, given that the enhancement calculation has in practical terms to be done by a computer code rather than manually. In this process the coordinate n_x is initially set at a very low value, and then increased progressively until $n_x = r/2$. At each value of n_x Equation (46) is used with $\theta = 0$ to give:

$$\psi_1 = \left(\lambda_x \frac{1}{2n_x} + \lambda_y r) \right) / \left(\frac{1}{\sin\gamma\cos\gamma} + \left(r - 2n_x \right) \right) \tag{50}$$

For a virtual angle of rotation $\delta\theta$, $\psi_2 \approx \psi_1$ and the virtual deflections are given by Equations (25) to (30) as:

$$\delta u_C = \delta\theta\psi_1 l/2 \tag{51}$$

$$\delta v_C = \delta v_{C_{y2}} = n_x \delta\theta\psi_1 l \tag{52}$$

$$\delta u_{T_{x1}} = -\delta\theta\left(\mu\tau - \psi_1\right) l \tag{53}$$

$$\delta v_{T_{y1}} = \delta v_{T_{y2}} = -2n_x \delta\theta\left(\mu\tau - \psi_1\right) l \tag{54}$$

The internal work is then given by a reduced form of Equation (32):

$$W_i = \delta\theta f_c l^3 \left(2\left(\lambda_x + 2\lambda_y r n_x\right)\left(\mu\tau - \psi_1\right) + \psi_1^2 (1 + 2rn_x) \right) \tag{55}$$

Hence the associated yield-line capacity is:

$$p = 6 f_c \left(2\left(\lambda_x + 2\lambda_y r n_x\right)\left(\mu\tau - \psi_1\right) + \psi_1^2 (1 + 2rn_x) \right) / \left(\left(3r - 2n_x\right) n_x \right) \tag{56}$$

For each assumed value of n_x a value of p is found, and when the minimum value has been detected n_x is refined until its optimum value has been determined to sufficient accuracy. This value is then fixed for use in the enhanced capacity calculations.

2.1.6 Subsequent cases

After some deflection Case **a1x** terminates when its conditions no longer apply, either because of the fracture of some reinforcement, or by loss of the mid-yield-line concrete stress block. As deflections increase further a range of different possibilities, each of which is characterized by a variation of Equation (46), has to be checked for validity at each deflection value. If the general form of the in-plane equilibrium Equation (13), which has already been specialized to Equation (46) for Case **a1x**, is expressed as:

$$a\psi_1^2 + b\psi_1 + c = 0 \tag{57}$$

then the expressions for the coefficients a, b and c of the in-plane equilibrium equations for each of these cases are shown in Tables 2, 3 and 4.

Case	$a\psi_1^2 + b\psi_1 + c = 0$				
	a	b		c	
a1x		$\left(\frac{1}{\sin\gamma\cos\gamma} + (r - 2n_x)\right)$		$-\frac{\theta n_x}{2}\left(\frac{1}{2\sin\gamma\cos\gamma} + (r - 2n_x)\right)$	$-\left(\lambda_x \frac{1}{2n_x} + \lambda_y r\right)$
a1x'		$\left(\frac{1}{\sin\gamma\cos\gamma} + (r - 2n_x)\right)$		$-\frac{\theta n_x}{2}\left(\frac{1}{2\sin\gamma\cos\gamma} + (r - 2n_x)\right)$	$-\left(\lambda_x \frac{1}{2n_x} + 2\lambda_y n_x\right)$
a1x*		$\left(\frac{1}{\sin\gamma\cos\gamma} + (r - 2n_x)\right)$	$-\lambda_x \frac{1}{\theta n_x^2}$	$-\frac{\theta n_x}{2}\left(\frac{1}{2\sin\gamma\cos\gamma} + (r - 2n_x)\right)$	$-\left(\lambda_x \frac{1}{\theta^2 n_x^2}(\eta_x - \theta\mu\tau) + \lambda_y r\right)$
a1x'*		$\left(\frac{1}{\sin\gamma\cos\gamma} + (r - 2n_x)\right)$	$-\lambda_x \frac{1}{\theta n_x^2}$	$-\frac{\theta n_x}{2}\left(\frac{1}{2\sin\gamma\cos\gamma} + (r - 2n_x)\right)$	$-\left(\lambda_x \frac{1}{\theta^2 n_x^2}(\eta_x - \theta\mu\tau) + 2\lambda_y n_x\right)$
a1x**		$\left(\frac{1}{\sin\gamma\cos\gamma} + (r - 2n_x)\right)$	$-\lambda_y \frac{4}{\theta}$	$-\frac{\theta n_x}{2}\left(\frac{1}{2\sin\gamma\cos\gamma} + (r - 2n_x)\right)$	$-\left(\lambda_x \frac{1}{2n_x} + 2\lambda_y \frac{1}{\theta^2 n_x}(\eta_y - 2n_x\mu\tau\theta)\right)$
a1x***		$\left(\frac{1}{\sin\gamma\cos\gamma} + (r - 2n_x)\right)$	$-\lambda_x \frac{1}{\theta n_x^2} - \lambda_y \frac{4}{\theta}$	$-\frac{\theta n_x}{2}\left(\frac{1}{2\sin\gamma\cos\gamma} + (r - 2n_x)\right)$	$-\left(\lambda_x \frac{1}{\theta^2 n_x^2}(\eta_x - \theta\mu\tau) + 2\lambda_y \frac{1}{\theta^2 n_x}(\eta_y - 2n_x\mu\tau\theta)\right)$
a2x		$\left(\frac{1}{\sin\gamma\cos\gamma} + (r - 2n_x)\right)$	$+\lambda_x \frac{1}{\theta n_x^2} + \lambda_y \frac{4}{\theta}$	$-\frac{\theta n_x}{2}\left(\frac{1}{2\sin\gamma\cos\gamma} + (r - 2n_x)\right)$	$-\left(\lambda_x(\frac{1}{2n_x} + \frac{\mu\tau}{\theta n_x^2}) + \lambda_y(r + \frac{4\mu\tau}{\theta})\right)$
a2x'		$\left(\frac{1}{\sin\gamma\cos\gamma} + (r - 2n_x)\right)$	$+\lambda_x \frac{1}{\theta n_x^2} + \lambda_y \frac{4}{\theta}$	$-\frac{\theta n_x}{2}\left(\frac{1}{2\sin\gamma\cos\gamma} + (r - 2n_x)\right)$	$-\left(\lambda_x(\frac{1}{2n_x} + \frac{\mu\tau}{\theta n_x^2}) + \lambda_y(2n_x + \frac{4\mu\tau}{\theta})\right)$
a2x*		$\left(\frac{1}{\sin\gamma\cos\gamma} + (r - 2n_x)\right)$	$+\lambda_y \frac{4}{\theta}$	$-\frac{\theta n_x}{2}\left(\frac{1}{2\sin\gamma\cos\gamma} + (r - 2n_x)\right)$	$-\left(\lambda_x \frac{\eta_x}{\theta^2 n_x^2} + \lambda_y(r + \frac{4\mu\tau}{\theta})\right)$
a2x'*		$\left(\frac{1}{\sin\gamma\cos\gamma} + (r - 2n_x)\right)$	$+\lambda_y \frac{4}{\theta}$	$-\frac{\theta n_x}{2}\left(\frac{1}{2\sin\gamma\cos\gamma} + (r - 2n_x)\right)$	$-\left(\lambda_x \frac{\eta_x}{\theta^2 n_x^2} + \lambda_y(2n_x + \frac{4\mu\tau}{\theta})\right)$
a2x**		$\left(\frac{1}{\sin\gamma\cos\gamma} + (r - 2n_x)\right)$	$+\lambda_x \frac{1}{\theta n_x^2}$	$-\frac{\theta n_x}{2}\left(\frac{1}{2\sin\gamma\cos\gamma} + (r - 2n_x)\right)$	$-\left(\lambda_x(\frac{1}{2n_x} + \frac{\mu\tau}{\theta n_x^2}) + \lambda_y \frac{2\eta_y}{\theta^2 n_x}\right)$
a2x***		$\left(\frac{1}{\sin\gamma\cos\gamma} + (r - 2n_x)\right)$		$-\frac{\theta n_x}{2}\left(\frac{1}{2\sin\gamma\cos\gamma} + (r - 2n_x)\right)$	$-\left(\lambda_x \frac{\eta_x}{\theta^2 n_x^2} + \lambda_y \frac{2\eta_y}{\theta^2 n_x}\right)$

Table 2: In-plane equilibrium equations for different possible x-aligned cases. Cases with concrete stress blocks on central and diagonal yield lines.

Case	$a\psi_1^2 + b\psi_1 + c = 0$		
	a	b	c
b1x	$\frac{1}{\sin\gamma\cos\gamma}$		$-\left(\lambda_x\frac{\theta}{2}+\lambda_y r n_x\theta\right)$
b1x'	$\frac{1}{\sin\gamma\cos\gamma}$		$-\left(\lambda_x\frac{\theta}{2}+\lambda_y 2n_x^2\theta\right)$
b1x*	$\frac{1}{\sin\gamma\cos\gamma}$	$-\lambda_x\frac{1}{n_x}$	$-\left(\frac{\lambda_x}{n_x}\left(\frac{\eta_x}{\theta}-\mu\tau\right)+\lambda_y r n_x\theta\right)$
b1x'*	$\frac{1}{\sin\gamma\cos\gamma}$	$-\lambda_x\frac{1}{n_x}$	$-\left(\frac{\lambda_x}{n_x}\left(\frac{\eta_x}{\theta}-\mu\tau\right)+2\lambda_y n_x^2\theta\right)$
b1x**	$\frac{1}{\sin\gamma\cos\gamma}$	$-4\lambda_y n_x$	$-\left(\lambda_x\frac{\theta}{2}+\lambda_y(\frac{2\eta_y}{\theta}-4n_x\mu\tau)\right)$
b1x***	$\frac{1}{\sin\gamma\cos\gamma}$	$-\lambda_x\frac{1}{n_x}-4\lambda_y n_x$	$-\left(\frac{\lambda_x}{n_x}\left(\frac{\eta_x}{\theta}-\mu\tau\right)+\lambda_y\left(\frac{2\eta_y}{\theta}-4n_x\mu\tau\right)\right)$
b2x	$\frac{1}{\sin\gamma\cos\gamma}$	$+\lambda_x\frac{1}{n_x}+4\lambda_y n_x$	$-\left(\lambda_x\left(\frac{\theta}{2}+\frac{\mu\tau}{n_x}\right)+\lambda_y n_x(r\theta+4\mu\tau)\right)$
b2x'	$\frac{1}{\sin\gamma\cos\gamma}$	$+\lambda_x\frac{1}{n_x}+4\lambda_y n_x$	$-\left(\lambda_x\left(\frac{\theta}{2}+\frac{\mu\tau}{n_x}\right)+\lambda_y n_x(2n_x\theta+4\mu\tau)\right)$
b2x*	$\frac{1}{\sin\gamma\cos\gamma}$	$+4\lambda_y n_x$	$-\left(\lambda_x\frac{\eta_x}{n_x\theta}+\lambda_y n_x(r\theta+4\mu\tau)\right)$
b2x'*	$\frac{1}{\sin\gamma\cos\gamma}$	$+4\lambda_y n_x$	$-\left(\lambda_x\frac{\eta_x}{n_x\theta}+\lambda_y n_x(2n_x\theta+4\mu\tau)\right)$
b2x**	$\frac{1}{\sin\gamma\cos\gamma}$	$+\lambda_x\frac{1}{n_x}$	$-\left(\lambda_x\left(\frac{\theta}{2}+\frac{\mu\tau}{n_x}\right)+\lambda_y\frac{2\eta_y}{\theta}\right)$
b2x***	$\frac{1}{\sin\gamma\cos\gamma}$		$-\left(\lambda_x\frac{\eta_x}{n_x\theta}+\lambda_y\frac{2\eta_y}{\theta}\right)$

Table 3: In-plane equilibrium equations for different possible x-aligned cases. Cases with triangular concrete stress blocks on diagonal yield lines.

Case	$a\psi_1^2 + b\psi_1 + c = 0$				
	a	***b***		***c***	
cx		$\frac{2\tau}{\sin\gamma\cos\gamma}$	$+\frac{\lambda_x}{n_x}+4\lambda_y n_x$	$-\left(\frac{\tau^2}{\sin\gamma\cos\gamma}\right)$	$-\left(\lambda_x\left(\frac{\theta}{2}+\frac{\mu\tau}{n_x}\right)+\lambda_y n_x(r\theta+4\mu\tau)\right)$
cx'		$\frac{2\tau}{\sin\gamma\cos\gamma}$	$+\frac{\lambda_x}{n_x}+4\lambda_y n_x$	$-\left(\frac{\tau^2}{\sin\gamma\cos\gamma}\right)$	$-\left(\lambda_x\left(\frac{\theta}{2}+\frac{\mu\tau}{n_x}\right)+\lambda_y n_x(2n_x\theta+4\mu\tau)\right)$
cx*		$\frac{2\tau}{\sin\gamma\cos\gamma}$	$+4\lambda_y n_x$	$-\left(\frac{\tau^2}{\sin\gamma\cos\gamma}\right)$	$-\left(\lambda_x\frac{\eta_x}{n_x\theta}+\lambda_y n_x(r\theta+4\mu\tau)\right)$
cx'*		$\frac{2\tau}{\sin\gamma\cos\gamma}$	$+4\lambda_y n_x$	$-\left(\frac{\tau^2}{\sin\gamma\cos\gamma}\right)$	$-\left(\lambda_x\frac{\eta_x}{n_x\theta}+\lambda_y n_x(2n_x\theta+4\mu\tau)\right)$
cx**		$\frac{2\tau}{\sin\gamma\cos\gamma}$	$+\frac{\lambda_x}{n_x}$	$-\left(\frac{\tau^2}{\sin\gamma\cos\gamma}\right)$	$-\left(\lambda_x\left(\frac{\theta}{2}+\frac{\mu\tau}{n_x}\right)+\lambda_y\frac{2\eta_y}{\theta}\right)$
cx***		$\frac{2\tau}{\sin\gamma\cos\gamma}$		$-\left(\frac{\tau^2}{\sin\gamma\cos\gamma}\right)$	$-\left(\lambda_x\frac{\eta_x}{n_x\theta}+\lambda_y\frac{2\eta_y}{\theta}\right)$

Table 4: In-plane equilibrium equations for different possible x-aligned cases. Cases with trapezoidal concrete stress blocks on diagonal yield lines.

2.2 The *y*-aligned mechanism

As the reinforcement strength f_{px} in the *x*-direction (or its dimensionless parameter λ_x) increases relative to f_{py} the optimum value of n_x increases until, as illustrated in Figure 6, it becomes greater than $r/2$. The optimum mechanism then becomes *y*-aligned, with n_y as the dimension which defines the geometry. The in-plane equilibrium equation at infinitesimal deflection now gives:

$$\psi_1 = \left(\lambda_x + \lambda_y \frac{r^2}{2n_y} \right) / \left(\frac{r}{\sin\gamma\cos\gamma} + \left(1 - 2n_y\right) \right) \tag{58}$$

For a virtual angle of rotation $\delta\theta$, $\psi_2 \approx \psi_1$ the virtual deflections are now:

$$\delta u_C = \delta u_{C_{x2}} = \delta\theta\psi_1 l / 2 \tag{59}$$

$$\delta v_C = \frac{r}{4n_y}\delta\theta\psi_1 l \tag{60}$$

$$\delta u_{T_{x1}} = \delta u_{T_{x2}} = -\delta\theta\left(\mu\tau - \psi_1\right) l \tag{61}$$

$$\delta v_{T_{y1}} = -\frac{r}{2n_y}\delta\theta\left(\mu\tau - \psi_1\right) l \tag{62}$$

The internal work is then given by:

$$W_i = \delta\theta f_c l^3 \left(2\left(\lambda_x + \lambda_y \frac{r^2}{2n_y} \right)\left(\mu\tau - \psi_1\right) + \psi_1^2 (1 + \frac{r^2}{2n_y}) \right) \tag{63}$$

The loss of potential of the external uniformly distributed load p is now:

$$W_e = pl^3 \left(\frac{1}{2} - \frac{n_y}{3} \right) \delta\theta \frac{r^2}{2} \tag{64}$$

Hence the associated yield-line capacity is:

$$p = 12 f_c \left(2\left(\lambda_x + \lambda_y \frac{r^2}{2n_y} \right)\left(\mu\tau - \psi_1\right) + \psi_1^2 (1 + \frac{r^2}{2n_y}) \right) / \left(\left(3 - 2n_y\right) r^2 \right) \tag{65}$$

Again it is convenient to optimize the yield-line pattern iteratively rather than algebraically, and this fixes both the yield-line capacity and the mechanism geometry for subsequent deflection of the slab. The initial in-plane equilibrium equation, based on the force system shown in Figure 11, is:

$$\left(T_{x1}+T_{x2}\right)\cos\gamma+T_{y1}\sin\gamma=C+C_{x2}\cos\gamma \tag{66}$$

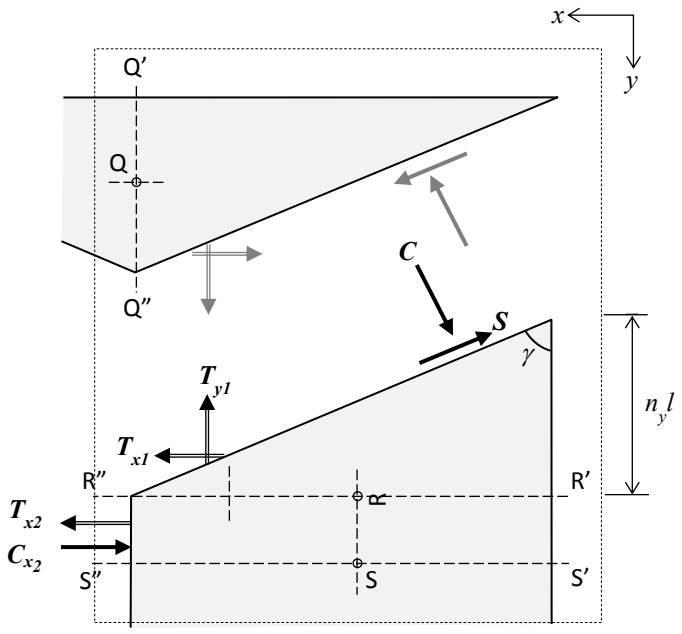

Figure 11: The horizontal force system between facets along the yield lines, for y-aligned mechanisms.

For the initial case **a1y**, in which there has been no reinforcement fracture and concrete stress blocks exist on all yield lines, the force components are:

$$C=\frac{f_c l n_y}{2cos\gamma}\left(2z_1-\frac{\theta r l}{4}\right) \tag{67}$$

$$C_{x2}=f_c l\left(\frac{1}{2}-n_y\right)\left(z_1-\frac{\theta r l}{4}\right) \tag{68}$$

$$T_{y1}=f_{py} l\frac{r}{2} \tag{69}$$

$$T_{x1}=f_{px} l n_y \tag{70}$$

$$T_{x2}=f_{px} l\left(\frac{1}{2}-n_y\right) \tag{71}$$

For Case **a1y**, and using the dimensionless relationships defined in Equations (42) to (45), Equation (66) becomes:

$$\psi_1\left(\frac{r}{\sin\gamma\cos\gamma}+\left(1-2n_y\right)\right)-\frac{\theta r}{4}\left(\frac{r}{2\,sin\gamma\cos\gamma}+\left(1-2n_y\right)\right)-\left(\lambda_x+\lambda_y\frac{r^2}{2n_y}\right)=0 \tag{72}$$

In the general form shown in Equation (57) the terms within the in-plane equilibrium equations for all of the subsequent *y*-aligned cases defined in Table 5 are shown in Tables 6, 7 and 8.

Compression block		Reinforcement mesh fracturing					
		None	Central x (all)	Diagonal y	Central x + diagonal y	Central x + Diagonal x	Diagonal x and y
Full	above mesh	**a1y**	**a1y'**	**a1y***	**a1y'***	**a1y****	**a1y*****
	below mesh	**a2y**	**a2y'**	**a2y***	**a2y'***	**a2y****	**a2y*****
Triangular	above mesh	**b1y**	**b1y'**	**b1y***	**b1y'***	**b1y****	**b1y*****
	below mesh	**b2y**	**b2y'**	**b2y***	**b2y'***	**b2y****	**b2y*****
Trapezoidal		**cy**	**cy'**	**cy***	**cy'***	**cy****	**cy*****

Table 5: Combinations of compression block configuration and rebar fracture for y-aligned cases.

The expression for loss of potential of the external uniformly distributed load p is:

$$W_e = pl^3\left(\frac{1}{2}-\frac{n_y}{3}\right)\theta\frac{r^2}{2} \tag{73}$$

The aggregate internal work is:

$$W_i = -4\left(T_{x1}u_{T_{x1}} + T_{x2}u_{T_{x2}} + T_{y1}v_{T_{y1}} + C(u_C\cos\gamma + v_C\sin\gamma) + C_{x2}u_{C_{x2}}\right) \tag{74}$$

The enhanced load capacity for the assumed value of θ is therefore:

$$p = \frac{12W_i}{l^3\theta\left(3-2n_y\right)r^2} \tag{75}$$

Case	$a\psi_1^2 + b\psi_1 + c = 0$				
	a	b		c	
a1y		$\left(\frac{r}{\sin\gamma\cos\gamma} + (1-2n_y)\right)$		$-\frac{\theta r}{4}\left(\frac{r}{2\sin\gamma\cos\gamma} + (1-2n_y)\right)$	$-\left(\lambda_x + \lambda_y\frac{r^2}{2n_y}\right)$
a1y'		$\left(\frac{r}{\sin\gamma\cos\gamma} + (1-2n_y)\right)$		$-\frac{\theta r}{4}\left(\frac{r}{2\sin\gamma\cos\gamma} + (1-2n_y)\right)$	$-\left(2n_y\lambda_x + \lambda_y\frac{r^2}{2n_y}\right)$
a1y*		$\left(\frac{r}{\sin\gamma\cos\gamma} + (1-2n_y)\right)$	$-\lambda_y\frac{2r}{\theta n_y}$	$-\frac{\theta r}{4}\left(\frac{r}{2\sin\gamma\cos\gamma} + (1-2n_y)\right)$	$-\left(\lambda_x + \lambda_y\frac{2}{\theta^2 n_y}(\eta_y n_y - \mu\tau r\theta)\right)$
a1y'*		$\left(\frac{r}{\sin\gamma\cos\gamma} + (1-2n_y)\right)$	$-\lambda_y\frac{2r}{\theta n_y}$	$-\frac{\theta r}{4}\left(\frac{r}{2\sin\gamma\cos\gamma} + (1-2n_y)\right)$	$-\left(2n_y\lambda_x + \lambda_y\frac{2}{\theta^2 n_y}(2\eta_y n_y - \mu\tau r\theta)\right)$
a1y**		$\left(\frac{r}{\sin\gamma\cos\gamma} + (1-2n_y)\right)$	$-\lambda_x\frac{2r}{\theta n_y}$	$-\frac{\theta r}{4}\left(\frac{r}{2\sin\gamma\cos\gamma} + (1-2n_y)\right)$	$-\left(\lambda_x\frac{2r}{\theta^2 n_y}(\eta_x - \mu\tau\theta) + \lambda_y\frac{r^2}{2n_y}\right)$
a1y***		$\left(\frac{r}{\sin\gamma\cos\gamma} + (1-2n_y)\right)$	$-\lambda_x\frac{2r}{\theta n_y} - \lambda_y\frac{2r}{\theta n_y}$	$-\frac{\theta r}{4}\left(\frac{r}{2\sin\gamma\cos\gamma} + (1-2n_y)\right)$	$-\left(\lambda_x\frac{2r}{\theta^2 n_y}(\eta_x - \mu\tau\theta) + \lambda_y\frac{2}{\theta^2 n_y}(2\eta_y n_y - \mu\tau r\theta)\right)$
a2y		$\left(\frac{r}{\sin\gamma\cos\gamma} + (1-2n_y)\right)$	$+\lambda_x\frac{8n_y}{\theta r} + \lambda_y\frac{2r}{\theta n_y}$	$-\frac{\theta r}{4}\left(\frac{r}{2\sin\gamma\cos\gamma} + (1-2n_y)\right)$	$-\left(\lambda_x(1 + \frac{8n_y\mu\tau}{\theta r}) + \lambda_y\frac{r}{2n_y}(r + \frac{4\mu\tau}{\theta})\right)$
a2y'		$\left(\frac{r}{\sin\gamma\cos\gamma} + (1-2n_y)\right)$	$+\lambda_x\frac{8n_y}{\theta r} + \lambda_y\frac{2r}{\theta n_y}$	$-\frac{\theta r}{4}\left(\frac{r}{2\sin\gamma\cos\gamma} + (1-2n_y)\right)$	$-\left(\lambda_x(2n_y + \frac{8n_y\mu\tau}{\theta r}) + \lambda_y\frac{r}{2n_y}(r + \frac{4\mu\tau}{\theta})\right)$
a2y*		$\left(\frac{r}{\sin\gamma\cos\gamma} + (1-2n_y)\right)$	$+\lambda_x\frac{8n_y}{\theta r}$	$-\frac{\theta r}{4}\left(\frac{r}{2\sin\gamma\cos\gamma} + (1-2n_y)\right)$	$-\left(\lambda_x(1 + \frac{8n_y\mu\tau}{\theta r}) + \lambda_y\frac{4\eta_y}{\theta^2}\right)$
a2y'*		$\left(\frac{r}{\sin\gamma\cos\gamma} + (1-2n_y)\right)$	$+\lambda_x\frac{8n_y}{\theta r}$	$-\frac{\theta r}{4}\left(\frac{r}{2\sin\gamma\cos\gamma} + (1-2n_y)\right)$	$-\left(\lambda_x(2n_y + \frac{8n_y\mu\tau}{\theta r}) + \lambda_y\frac{4\eta_y}{\theta^2}\right)$
a2y**		$\left(\frac{r}{\sin\gamma\cos\gamma} + (1-2n_y)\right)$	$+\lambda_y\frac{2r}{\theta n_y}$	$-\frac{\theta r}{4}\left(\frac{r}{2\sin\gamma\cos\gamma} + (1-2n_y)\right)$	$-\left(\lambda_x\frac{8\eta_x n_y}{\theta^2 r} + \lambda_y\frac{r}{2n_y}(r + \frac{4\mu\tau}{\theta})\right)$
a2y***		$\left(\frac{r}{\sin\gamma\cos\gamma} + (1-2n_y)\right)$		$-\frac{\theta r}{4}\left(\frac{r}{2\sin\gamma\cos\gamma} + (1-2n_y)\right)$	$-\left(\lambda_x\frac{8\eta_x n_y}{\theta^2 r} + \lambda_y\frac{4\eta_y}{\theta^2}\right)$

Table 6: In-plane equilibrium equations for different possible y-aligned cases. Cases with concrete stress blocks on central and diagonal yield lines.

Case	$a\psi_1^2 + b\psi_1 + c = 0$		
	a	b	c
b1y	$\frac{1}{\sin\gamma\cos\gamma}$		$-\left(\lambda_x\frac{\theta}{2}+\lambda_y\frac{r^2\theta}{4n_y}\right)$
b1y'	$\frac{1}{\sin\gamma\cos\gamma}$		$-\left(\lambda_x n_y\theta+\lambda_y\frac{r^2\theta}{4n_y}\right)$
b1y*	$\frac{1}{\sin\gamma\cos\gamma}$	$-\lambda_y\frac{r}{n_y}$	$-\left(\lambda_x\frac{\theta}{2}+\lambda_y\left(\frac{2\eta_y}{\theta}-\frac{\mu\tau r}{n_y}\right)\right)$
b1y'*	$\frac{1}{\sin\gamma\cos\gamma}$	$-\lambda_y\frac{r}{n_y}$	$-\left(\lambda_x n_y\theta+\lambda_y\left(\frac{2\eta_y}{\theta}-\frac{\mu\tau r}{n_y}\right)\right)$
b1y**	$\frac{1}{\sin\gamma\cos\gamma}$	$-\lambda_x\frac{4n_y}{r}$	$-\left(\lambda_x\frac{4n_y}{r}\left(\frac{\eta_x}{\theta}-\mu\tau\right)+\lambda_y\frac{r^2\theta}{4n_y}\right)$
b1y***	$\frac{1}{\sin\gamma\cos\gamma}$	$-\lambda_x\frac{4n_y}{r}-\lambda_y\frac{r}{n_y}$	$-\left(\lambda_x\frac{4n_y}{r}\left(\frac{\eta_x}{\theta}-\mu\tau\right)+\lambda_y\left(\frac{2\eta_y}{\theta}-\frac{\mu\tau r}{n_y}\right)\right)$
b2y	$\frac{1}{\sin\gamma\cos\gamma}$	$+\lambda_x\frac{4n_y}{r}+\lambda_y\frac{r}{n_y}$	$-\left(\lambda_x\left(\frac{\theta}{2}+\frac{4\mu\tau n_y}{r}\right)+\lambda_y\frac{r}{4n_y}(r\theta+4\mu\tau)\right)$
b2y'	$\frac{1}{\sin\gamma\cos\gamma}$	$+\lambda_x\frac{4n_y}{r}+\lambda_y\frac{r}{n_y}$	$-\left(\lambda_x\left(n_y\theta+\frac{4\mu\tau n_y}{r}\right)+\lambda_y\frac{r}{4n_y}(r\theta+4\mu\tau)\right)$
b2y*	$\frac{1}{\sin\gamma\cos\gamma}$	$+\lambda_x\frac{4n_y}{r}$	$-\left(\lambda_x\left(\frac{\theta}{2}+\frac{4\mu\tau n_y}{r}\right)+\lambda_y\frac{2\eta_y}{\theta}\right)$
b2y'*	$\frac{1}{\sin\gamma\cos\gamma}$	$+\lambda_x\frac{4n_y}{r}$	$-\left(\lambda_x\left(n_y\theta+\frac{4\mu\tau n_y}{r}\right)+\lambda_y\frac{2\eta_y}{\theta}\right)$
b2y**	$\frac{1}{\sin\gamma\cos\gamma}$	$+\lambda_y\frac{r}{n_y}$	$-\left(\lambda_x\frac{4n_y\eta_x}{r\theta}+\lambda_y\frac{r}{4n_y}(r\theta+4\mu\tau)\right)$
b2y***	$\frac{1}{\sin\gamma\cos\gamma}$		$-\left(\lambda_x\frac{4n_y\eta_x}{r\theta}+\lambda_y\frac{2\eta_y}{\theta}\right)$

Table 7: In-plane equilibrium equations for different possible y-aligned cases. Cases with triangular concrete stress blocks on diagonal yield lines.

Case	$a\psi_1^2 + b\psi_1 + c = 0$				
	a	***b***		***c***	
cy		$\frac{2\tau}{\sin\gamma\cos\gamma}$	$+\lambda_x\frac{4n_y}{r}+\lambda_y\frac{r}{n_y}$	$-\left(\frac{\tau^2}{\sin\gamma\cos\gamma}\right)$	$-\left(\lambda_x\left(\frac{\theta}{2}+\frac{4\mu\tau n_y}{r}\right)+\lambda_y\frac{r}{4n_y}(r\theta+4\mu\tau)\right)$
cy'		$\frac{2\tau}{\sin\gamma\cos\gamma}$	$+\lambda_x\frac{4n_y}{r}+\lambda_y\frac{r}{n_y}$	$-\left(\frac{\tau^2}{\sin\gamma\cos\gamma}\right)$	$-\left(\lambda_x\left(\theta n_y+\frac{4\mu\tau n_y}{r}\right)+\lambda_y\frac{r}{4n_y}(r\theta+4\mu\tau)\right)$
cy*		$\frac{2\tau}{\sin\gamma\cos\gamma}$	$+\lambda_x\frac{4n_y}{r}$	$-\left(\frac{\tau^2}{\sin\gamma\cos\gamma}\right)$	$-\left(\lambda_x\left(\frac{\theta}{2}+\frac{4\mu\tau n_y}{r}\right)+\lambda_y\frac{2\eta_y}{\theta}\right)$
cy'*		$\frac{2\tau}{\sin\gamma\cos\gamma}$	$+\lambda_x\frac{4n_y}{r}$	$-\left(\frac{\tau^2}{\sin\gamma\cos\gamma}\right)$	$-\left(\lambda_x\left(\theta n_y+\frac{4\mu\tau n_y}{r}\right)+\lambda_y\frac{2\eta_y}{\theta}\right)$
cy**		$\frac{2\tau}{\sin\gamma\cos\gamma}$	$+\lambda_y\frac{r}{n_y}$	$-\left(\frac{\tau^2}{\sin\gamma\cos\gamma}\right)$	$-\left(\lambda_x\frac{4n_y\eta_x}{r\theta}+\lambda_y\frac{r}{4n_y}(r\theta+4\mu\tau)\right)$
cy***		$\frac{2\tau}{\sin\gamma\cos\gamma}$		$-\left(\frac{\tau^2}{\sin\gamma\cos\gamma}\right)$	$-\left(\lambda_x\frac{4n_y\eta_x}{r\theta}+\lambda_y\frac{2\eta_y}{\theta}\right)$

Table 8: In-plane equilibrium equations for different possible y-aligned cases. Cases with trapezoidal concrete stress blocks on diagonal yield lines.

3. APPLICATION OF THE MODEL

Although there is insufficient space in this paper for a comprehensive practical study of the theory presented, it is appropriate to illustrate the key aspects of its application, and how its predictions compare with those of the existing BRE calculation in some examples which reflect practical design. The theory which has been developed in this paper deals only with slabs whose membrane action is changing whilst the triangular and trapezoidal slab facets, defined by the optimal yield-line mechanism, are deflecting. Although it provides maximum in-plane tensile stresses, which will trigger the almost instantaneous development of the transverse tension crack observed in most experiments, it does not cover the load capacity enhancement once this extra crack has developed. The theoretical extension for this phase will be covered in a subsequent paper; at that point it will be appropriate to perform parametric studies directly comparing it, the BRE and FRACOF methods, with test results which include the transverse tension crack.

3.1 Comparisons with the BRE method based on the Garston Test

As has been pointed-out earlier the ultimate aim of this development is to address tensile membrane action of composite slabs in fire conditions, when downstand steel beams have largely lost their strength at very high temperatures. Although these studies consider only the load capacity enhancement of concrete slabs at ambient temperature, the test cases use dimensions which are more typical of the concrete slabs used in composite construction than of those in normally-reinforced concrete. The ambient-temperature large-scale slab test at Garston, reported by Bailey *et al.* [25], is very useful in this respect. It was intended to represent a 9 m x 6 m corner-bay slab from the Cardington composite building. Assuming that the single unprotected downstand steel beam running centrally along the long-span of this slab would have lost all significant strength at high temperature, this beam was omitted from the Garston set-up. The average depth of the slab was 120 mm, and the mean effective depth of the A142 mesh was 69 mm. The dimensions of its supported edges were 9500 mm x 6460 mm, giving an aspect ratio of 1.4706. The compressive cube strength of the concrete on the day of the test was 52 MPa (equivalent to a cylinder strength f_{ck} of 42 MPa). From several tensile tests the undeformed (prismatic) mesh bars achieved an average tensile strength of about 580 MPa at a fracture strain of 12%. In these analyses the limiting crack-width at which reinforcement fractures is represented as an “equivalent fracture strain”, using the 200mm length between the anchor-points created by the welds between orthogonal bars as a gauge-length. This ignores the bond between concrete and reinforcement, and is therefore an inherently unconservative way of considering the limiting crack-width at which reinforcement fractures, because it ignores bond along the surfaces of bars. If the as-tested tensile fracture strain

of the bars is used in this context, then this represents fairly well the behaviour of slabs with undeformed bars; this applies to the composite slabs used at Cardington and in the subsequent Garston ambient-temperature test [25]. For slabs with deformed bars it would clearly be an over-ductile assumption. The optimum yield-line load capacity of the slab using this data is 2.30 kN/m^2, which was almost identical to its self-weight combined with that of the attached loading gear in the actual test. On further loading the slab achieved an enhanced total capacity of 4.81 kN/m^2, until sudden fracture across the mid-span short dimension occurred,. The test cases used here use this as their base case, which is referred to as "the Garston Test".

3.1.1 The effect of mesh ductility, aspect ratio and effective depth for isotropically reinforced slabs

A series of slabs based on the Garston Test details, but with different aspect ratios and mesh effective depths, have been tested using the new formulation, to illustrate the ways in which reinforcement fracture takes place as deformation of the yield-line pattern increases, and its effect on load capacity. In the absence of definitive guidance on the pull-out characteristics of reinforcing bars from discrete cracks in concrete, both the tested ductility value of 12% and a lower ductility of 4%, which might represent better the characteristics of deformed bars, have been used. This mesh has been located at both the original mean effective depth of 69mm and at 35mm from the top surface. Two extra aspect ratios, of 1.0 and 2.0, have been considered in addition to 1.4706 for the same "short" span l of 6.460m. With the optimum yield-line mechanism as a starting-point, deflections have been increased progressively, initially in Case a1x, for these slabs. The load capacity enhancement factors for the two different mesh effective depths have been plotted in Figures 12(a – f), in terms of mid-slab deflection normalized with respect to the mesh effective depth. In each case the BRE enhancements are plotted on the same graphs. It can be seen that, even before any mesh fracture has taken place, the rate of enhancement with deflection changes differently in the two methods, so that the BRE method gives higher predictions for square slabs and lower predictions for aspect ratio 2.0, with approximate parity, at least initially, for aspect ratio 1.4706. On each of the six graphs two enhancement curves are plotted, representing the different effective ductilities of 12% and 4% (or fracture crack-widths of 24mm and 8mm); this has no effect on the BRE method's calculated enhancement. It can be seen in each case that the peak enhancement, given either by sudden fracture of the central yield line mesh or by the initiation of "unzipping" across the diagonal yield lines, is considerably increased by the higher ductility. In the event of fracture across the central yield line a sudden loss of load capacity occurs, whereas the initiation of "unzipping" along diagonal yield lines causes the load capacity to begin reducing gradually from a peak with deflection.

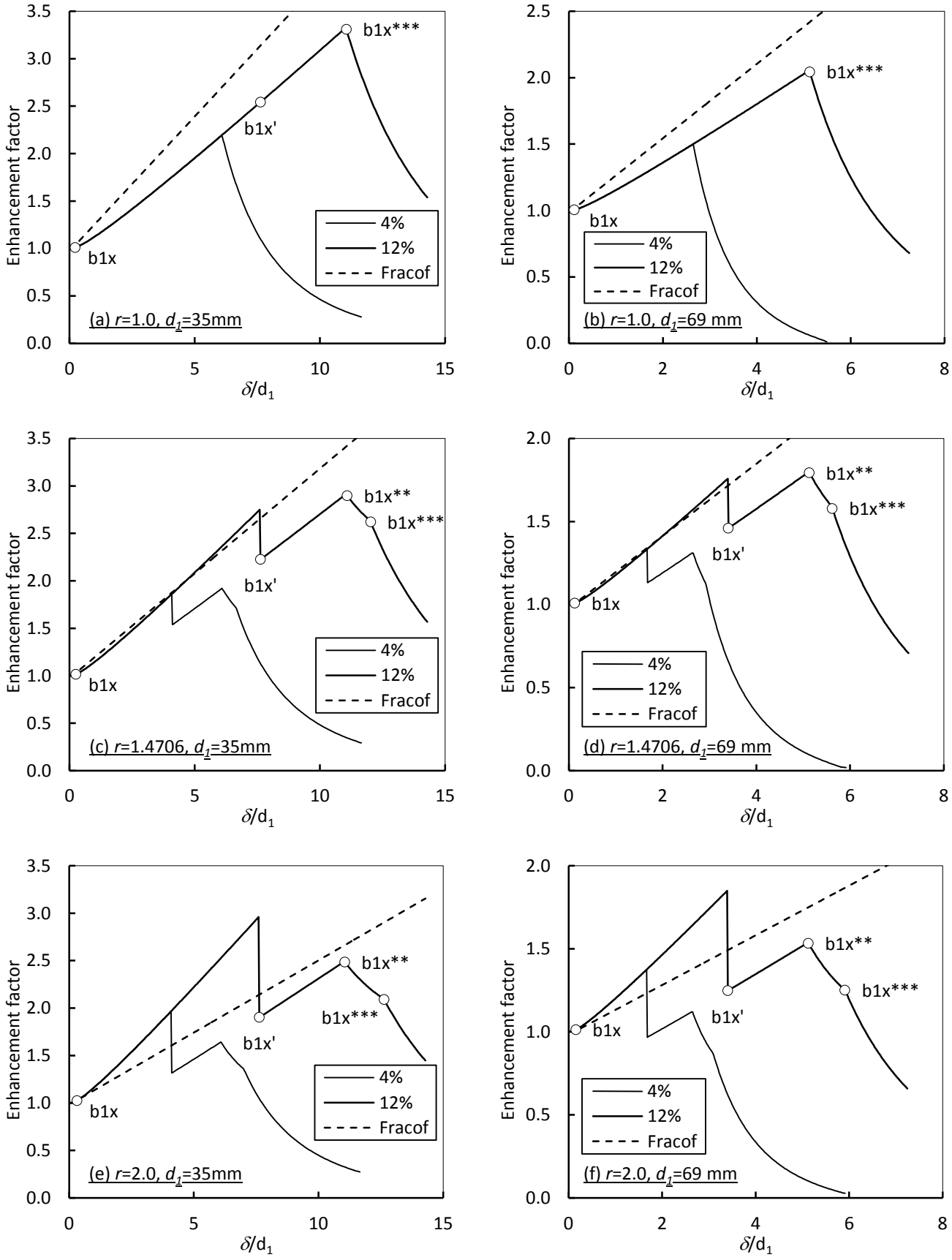

Figure 12: Slab capacity enhancement factors with displacement for slabs of width 6.46m and different aspect ratios and mesh effective depths.

The enhancement factors plotted for the cases with 12% ductility and 69 mm effective depth in Figures 12(a-f) are compared directly in Figure 13(a). The slabs all show similar behaviour in qualitative terms, with the greatest initial enhancements for the slabs of the higher aspect ratios.

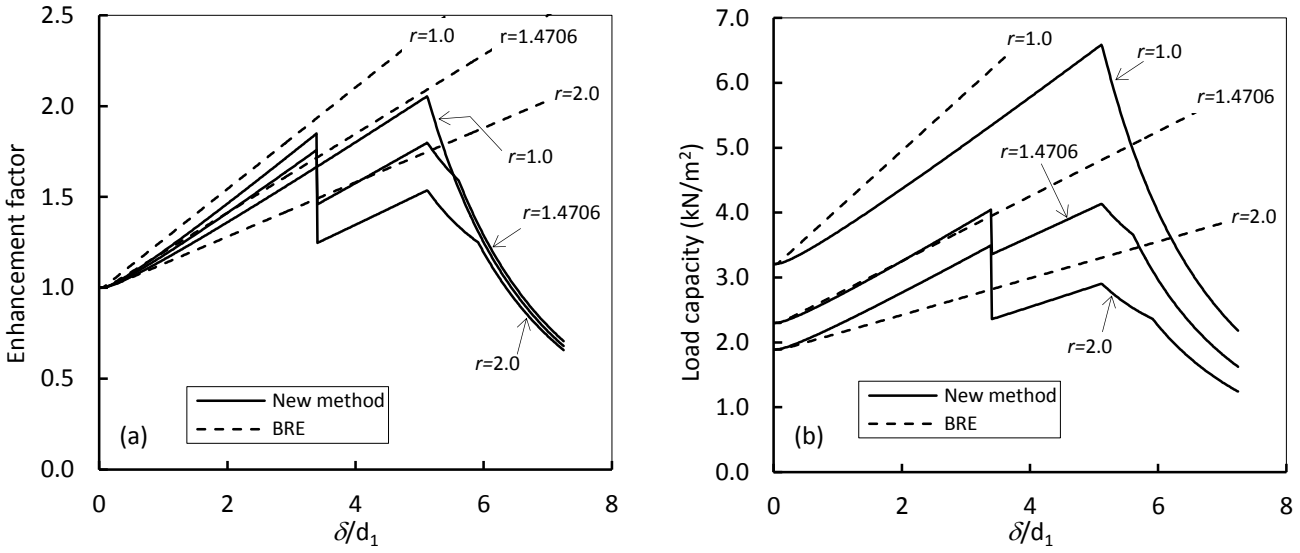

Figure 13: Variation of capacity with aspect ratio for isotropically-reinforced slabs: (a) Dimensionless enhancement factor; (b) Actual capacity for the particular slab cross-section.

This seems superficially counter-intuitive, but is rationalized by considering the absolute values of load capacity plotted against deflection which are shown in Figure 13(b); the small-deflection yield-line capacities themselves decline markedly with increasing aspect ratio, and the curves showing how this capacity is increased at any finite deflection remain roughly parallel to one another, so that a square slab is always the strongest and the slab with the highest aspect ratio is always the weakest at any particular deflection.

3.1.2 Variation of force resultants and in-plane stresses

As the deflection of the yield-line mechanism increases, causing the concrete stress block to change its shape and position and the reinforcing mesh to fracture either abruptly across the central yield line or progressively across the diagonal yield lines, the resultant forces given by Equations (37-41) or (67-71), which are shown in Figures 10 and 11, change. Their variation is shown in Figure 14 for a single case, of the Garston 9500 mm x 6360 mm slab (aspect ratio 1.4706) defined above with A142 mesh of an effective ductility of 12%, placed at an average depth of 69mm.

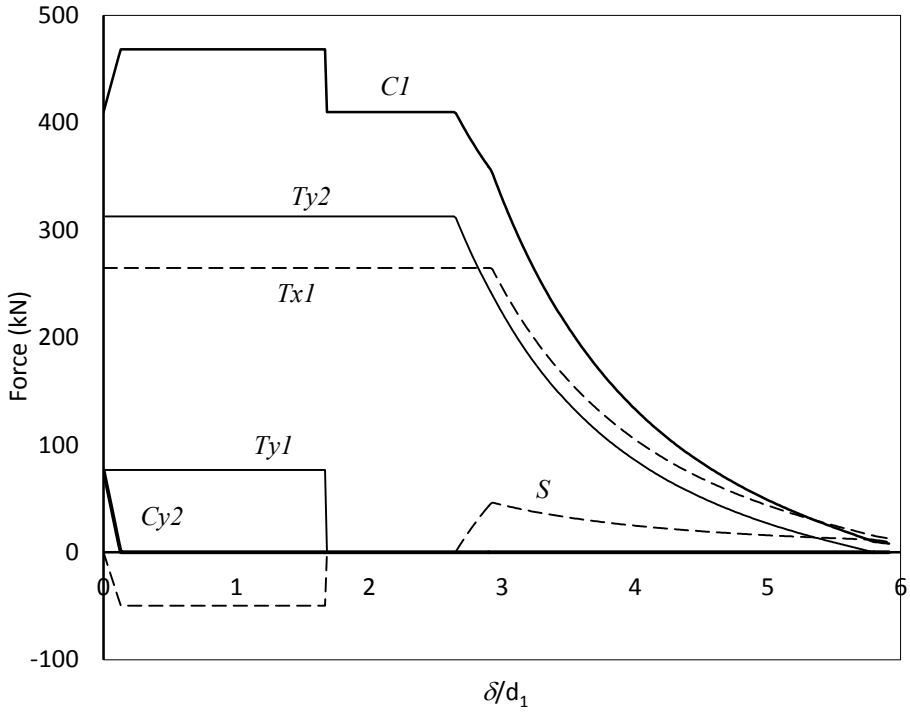

Figure 14: Variation of the resultant forces on yield lines with deflection of the slab (r=1.4706, d_1=69mm, effective ductility 4%).

The values of the force resultants can be used to calculate the net in-plane bending moments and forces acting on the slab cross-sections passing through the points Q, R and S, shown in Figures 10 and 11. These are the cross-sections at which it is most likely that a through-depth tensile failure of the concrete will take place, on the basis of evidence from test results over many years. Assuming that both the concrete and steel mesh crossing these as-yet uncracked cross-sections are elastic, the normal linear-elastic engineers' bending relationships can be used to calculate the values of tensile and compressive stress acting on these cross-sections. In accordance with the general concept of Tensile Membrane Action the maximum compressive stress is always found to be at the edge of the slab, and the maximum tension at the central yield line (the yield-line intersection for R and S). The maximum in-plane tensile stresses on these cross-sections are plotted for the Garston slab example in Figure. 15. If the initiation of through-depth tension cracks is considered as significant, as it has been in the existing simplified methods, then a limiting value of concrete tensile strength (either based on test or an empirical value within the range of tabulated values given in Table 3.1 of Eurocode 2 Part 1-1 [29]) can be used to determine the deflection at which the through-depth crack occurs. For concrete of cylinder strength 42MPa the mean tensile strength is quoted as lying in the range 2.52-4.67 MPa, which suggests that the central through-depth crack could be initiated fairly early in the deflection for this particular case, and a new mechanism which includes this crack would then take over.

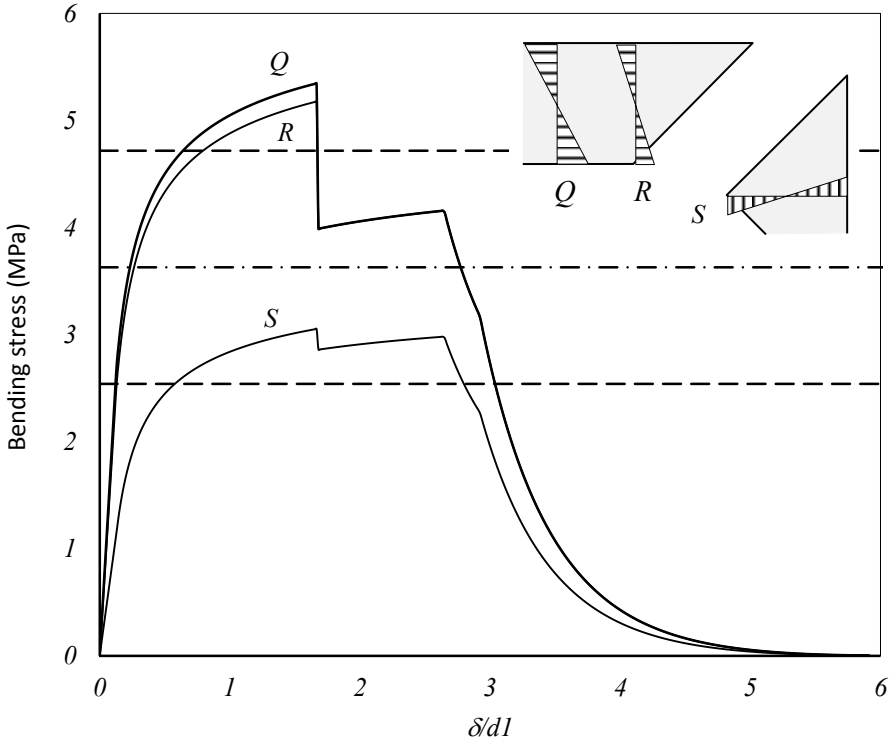

Figure 15: Variation of the maximum tensile in-plane bending stresses on yield lines with deflection of the slab (r=1.4706, d_1=69 mm, ductility 4%).

3.1.3 Variation of the initial yield-line mechanism with orthotropy of reinforcement

To illustrate the change of yield-line mechanism as the orthotropy ratio $\Omega = f_{py} / f_{px}$ rises the change of geometry of the yield-line mechanism, as indicated by the values of n_x and n_y , is plotted in Figure 16(a).

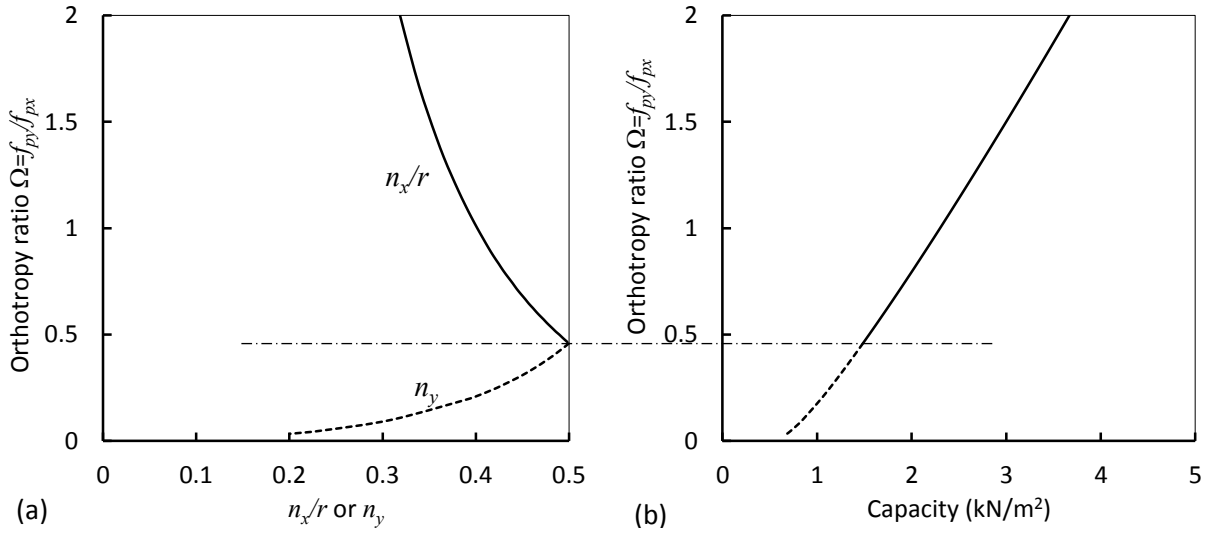

Fig. 1: Optimal x- and y-aligned yield-line mechanisms for a 9m x 6m slab with mesh effective depth 20 mm with different orthotropy ratios; (a) n_x and n_y; (b) Yield-line capacities.

At very small values of Ω the mechanism is y-aligned, and as it increases the optimal n_y value increases until it reaches 0.5. Beyond this point the mechanism is *x*-aligned, and n_x progressively decreases as Ω increases. The yield-line capacity variation with Ω is shown in Figure 16(b). Since f_{px} is held constant (with steel area of 142 mm^2/m in the *x*-direction) in these examples it is logical that the capacity value increases with Ω, but it is notable that the transition between *x*- and *y*-aligned mechanisms is continuous. For any particular case this yield-line mechanism fixes the geometry for the TMA phase.

3.1.4 The effect of orthotropy on tensile membrane action

It has been seen above that the optimal yield-line mechanism changes as the orthotropy ratio changes. In order to examine the effect of orthotropy on the finite-deflection behaviour the Garston Slab, of aspect ratio 1.4706 is given a range of Ω values by keeping the *y*-direction reinforcement constant at 142 mm^2/m and increasing the *x*-direction reinforcement through integer bar sizes from 6 mm upwards, keeping the spacing at 200 mm. The *x*-direction bar areas per metre run, shown on the enhancement plots in Figures 17(a) and 17(b) are therefore approximately 142, 192, 251, 318, 393, 475 and 565 mm^2/m, giving Ω values of 1.0, 0.73, 0.56, 0.44, 0.36, 0.30 and 0.25. The transition between x- and y-aligned mechanisms is at an *x*-direction bar area of 311 mm^2/m (Ω =0.457), which can be seen from Figures 17(a) and 17(b) to give the highest peak enhancement factor. The deflections which cause the peak capacities do not vary significantly with the orthotropy factor.

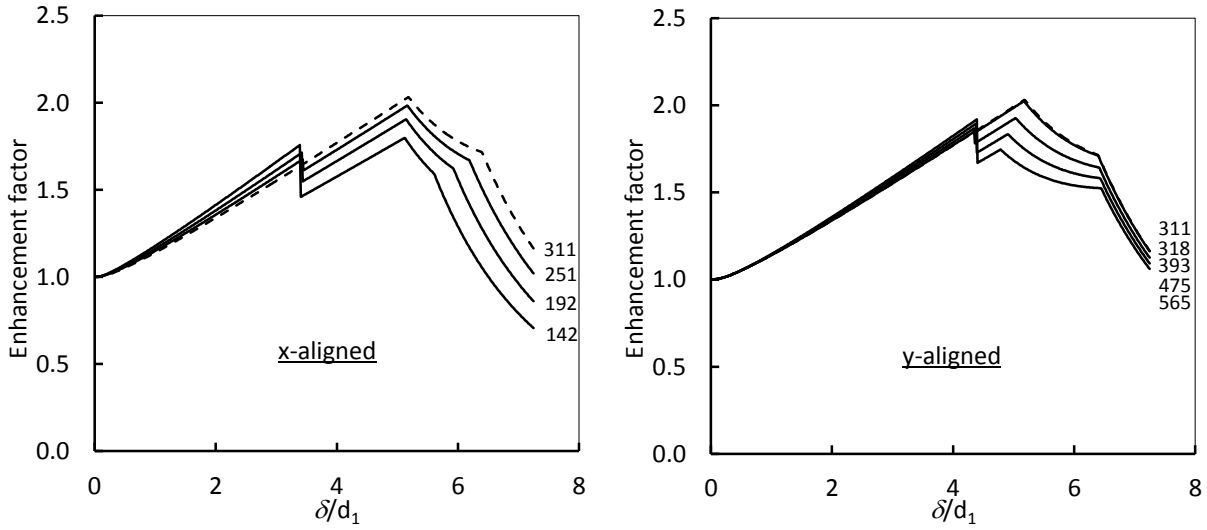

Figure 17: Enhancement for orthotropic slabs with y-reinforcement constant at 142 mm^2/m; x-reinforcement areas/m marked on curves. (a) x-aligned mechanisms. (b) y-aligned mechanisms.

The maximum tensile bending stresses at the points Q, half-way along the long span, irrespective of the alignment of the yield-line mechanism, are shown for each of the orthotropic reinforcement arrangements in Figure 18. It is clear that these tensile stresses increase as the *x*-direction reinforcement area increases. From the intercepts of these curves with the Eurocode 2 tensile strength range it is clear that, for the structural parameter values (particularly steel strength) of the Garston Test, the transverse through-depth crack will form at very low deflections.

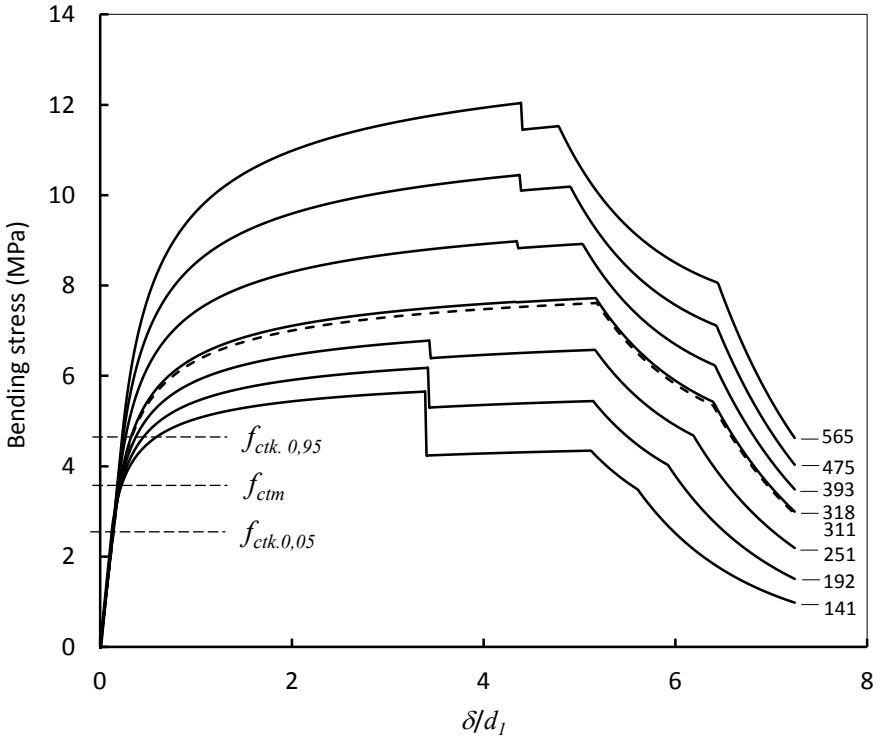

Figure 18: Variation of the maximum tensile in-plane bending stresses at position Q with deflection of the slab (r=1.4706, d_1=69 mm, ductility 12%) for different areas of x-reinforcement per metre, keeping y-reinforcement constant at 141.2 mm^2/m. The Eurocode 2 tensile strength range is indicated.

3.2 Comparisons against tests which do not form a mid-span tension crack

It is generally desirable to test new methods against load-deflection tests, but the problem in selecting suitable tests for comparison with the formulation developed in this paper is that this is specifically for cases in which no transverse through-depth tension crack has formed. A survey of tests carried out by previous researchers shows that transverse tension cracking, either at mid-span or from the yield-line intersection, occurred in nearly all of them. Given that Figure 18 shows cases with fairly typical reinforcement and concrete strengths, this is not surprising. However, a series of model-scale tests with different aspect ratios and various degrees of orthotropy were carried out by Foster et al. [30]. At the extreme end of the range of orthotropy in this test series four tests gave no sign of transverse tensile cracking, and these are used for comparison. It should be noted that, for the details of these tests, the graph of maximum in-plane tensile stress at the three key locations in

the centre of the slabs, which is similar to Figure 18, shows peak tensile stresses which lie below the Eurocode range of concrete tensile strengths, so the fact that transverse cracks do not occur is predicted by the new method.

The slabs tested were all of width 550 mm, with lengths 850 mm and 1150 mm, giving respective aspect ratios of 1.545 and 2.091. Slab thicknesses were between 15 mm and 18 mm, and samples of the small-aggregate concrete were tested for each test, the cube strengths being between 36 and 41 MPa. The reinforcement consisted of 0.71 mm steel wire of which samples were tested before each test, at an even spacing of 12 mm for the x-direction bars and 60 mm for the y-direction bars (an orthotropy coefficient Ω of 0.20). The wires were not welded together at their intersections, but were interwoven at intervals so that the mesh layer was fairly uniform. In two of the tests (denoted as Tests 6 and 11) the wires were smooth-surfaced, but in the other two (denoted as Tests 8 and 14) the wires had been deformed by indentation along their lengths in order to achieve better bond with the concrete. For the plain wires a number of tensile tests carried out before the slab tests gave yield strengths in the region 252-269 MPa, with fracture ductility of around 20%. The deformed wires showed yield strengths in the range 242-248 MPa and ductility reduced to around 11%. Before each slab test further tensile tests were carried out on samples of the wires actually used in the test. Pure tensile tests on sawn slab strips including both plain and deformed wires were also carried out. These showed very different bond characteristics around the local concrete tension fracture; plain wires pulled-out by amounts between 8 mm and 23 mm, with no wire fracture observed in 3 of 12 tests. For the deformed wires the pull-out at fracture was between 0.9 mm and 3 mm, demonstrating the effectiveness of the indentations in creating a shear-bond between the wires and the concrete. In terms of the simple definition of effective fracture ductility used previously (fracture crack-width/transverse bar spacing) this is equivalent to very high percentage ductilities – although the transverse wires are not welded to the longitudinal wires, so there are no discrete anchor-points. For this reason it is more useful simply to consider the crack-width that causes wire fracture, rather than relating this to a finite anchored length, especially because the wire spacings in the orthogonal directions are very different in the tests used at this stage.

3.2.1 Tests on slabs with plain wire reinforcement

Tests 6 and 11 were on slabs reinforced with plain wire. The test records, in terms of applied load intensity against deflection in deflection-controlled tests, are shown in Figures 19(a) and 19(b). It can be seen from these that an initial peak load, which fairly rapidly declines over 10-12 mm of deflection, is caused by the formation of the yield-line mechanism which requires the tensile strength of the concrete to be overcome progressively along the yield lines as the maximum tensile strain moves along the yield lines from the central region towards the corners, and as the initial

bond of the wires to the concrete is overcome. Beyond this stage, in both cases, the progressive enhancement of the load capacity, characteristic of tensile membrane action, occurs. The load capacities predicted by both the new method and the existing BRE method are shown for comparison on the graphs for both aspect ratios. In the case of the new method a high effective ductility, given by a fracture crack-width of 10mm in both directions, has been assumed, although for plain wires this could be set much higher on the basis of the tests on sawn slabs. Both methods show a consistent enhancement with deflection, although these do not fit particularly well with the test results. For Figure 19(a) the two methods show almost identical enhancements, but for the lower aspect ratio in Figure 19(b) they diverge considerably, with the new method showing an enhancement gradient which is almost parallel to the test.

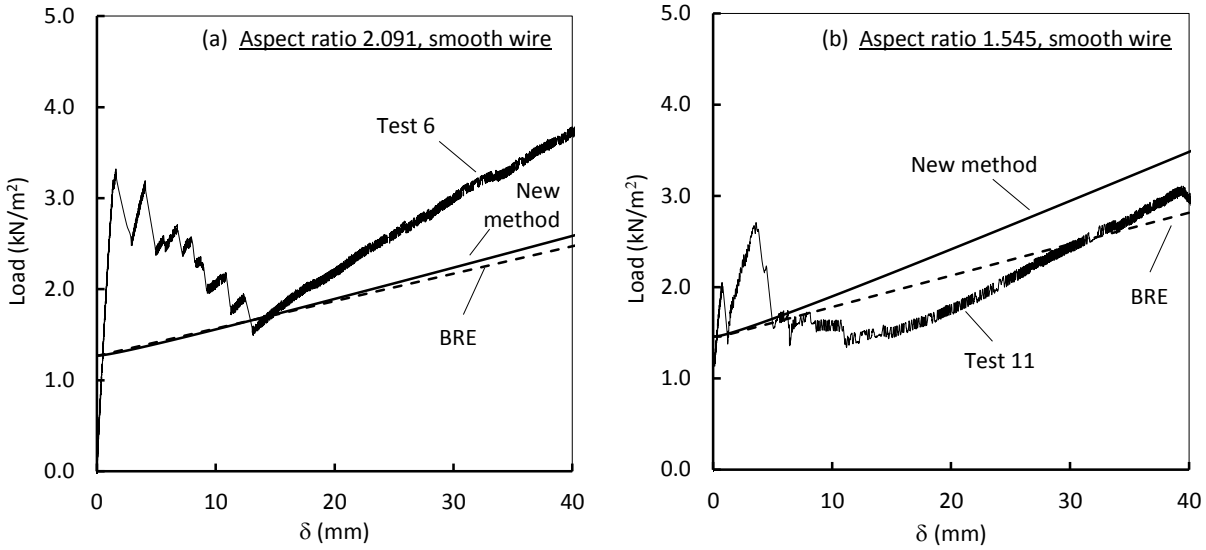

Figure 19: Comparison of predicted enhancements according to the new method and BRE with Foster et al. tests [30] using smooth reinforcement.

3.2.2 Tests on slabs with deformed wire reinforcement

Tests 8 and 14 were nominally identical to Tests 6 and 11, although some details, such as material strengths and the estimated value of effective depth, differed by a small amount. The key difference was that deformed wires were used as the mesh reinforcement. It can be seen from Figures 20(a) and 20(b) that the test behaviour was very different from that shown by slabs with smooth mesh. After the initial deflection of the order of 10-12 mm, beyond which the tensile strength of the concrete has been overcome, both aspect ratios show a steady progressive drop in load capacity. Enhanced load capacities given by the BRE method and the new method are shown on the two graphs. These predictions diverge considerably. For the BRE method the prediction is for a continuous increase of load capacity with deflection, which contrasts strongly with the decreasing capacity shown in the tests. However, the new method shows increasing load capacity up to a peak, the location of which is controlled by the assumed fracture ductility, beyond which the capacity

decreases as the y-direction wires fracture progressively along the diagonal yield lines. The fracture crack-widths for which curves are plotted are 1.2 mm, 1.8 mm and 2.1 mm, which are in the middle of the ductility range suggested by the direct tension tests on sawn specimens using deformed wire.

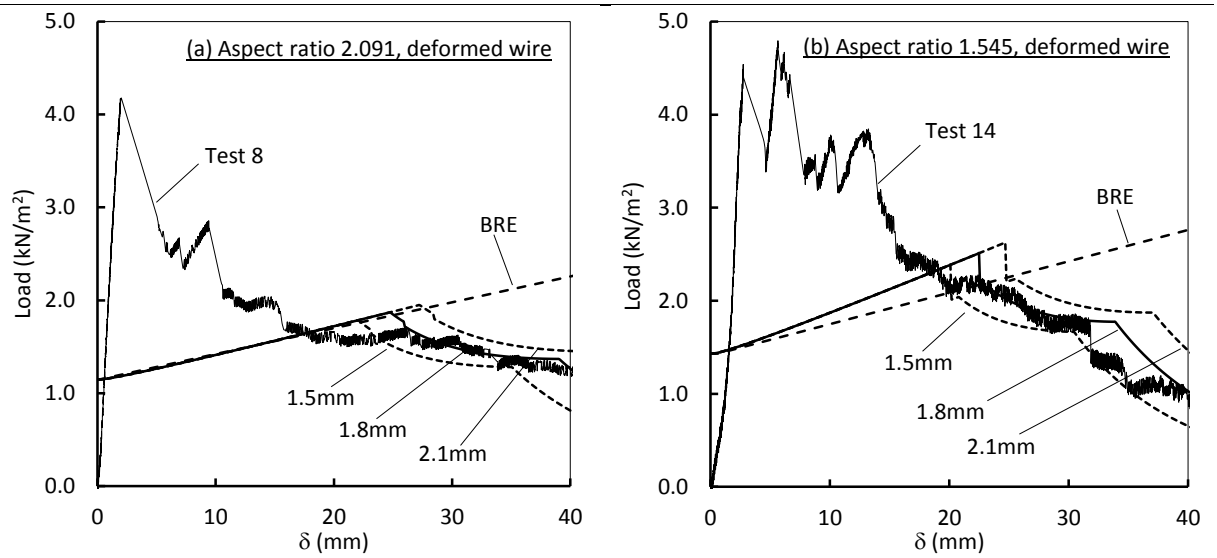

Figure 20: Comparison of predicted enhancements for different fracture crack-widths according to the new method and BRE with Foster et al. tests [30] using deformed reinforcement.

The decline of load capacity beyond the peak demonstrates the effect of "unzipping" of y-direction reinforcement along the diagonal yield lines. It is clear that the low fracture crack-widths caused by the deformed wire's bond characteristics cause dramatically different predictions from that of the BRE method, with the limiting load capacity being caused, essentially, by the initiation of reinforcement fracture due to relatively high bond between the wires and the concrete. The change from enhancement to falling load capacity compares very well with the experimental results for these tests. It is fortunate that the ductility data from the direct-tension tests on sawn slab-strips is available in these cases; wider application will clearly need reliable methods for determining fracture crack-widths at discrete cracks in lightly reinforced slabs.

4. CONCLUSION

The main fundamental difference between this treatment of tensile membrane action and previous studies is in its approach to the kinematics of a lightly-reinforced concrete slab which forms straight discrete yield lines at very small deflection. The geometry of interlocking flat facets involves there being a straight neutral axis on any yield line, which can be seen as the boundary between separated and contacting concrete surfaces. On any diagonal yield line this neutral axis is inclined to the plane of the slab surface, and this inclination increases as the slab deflection increases. Steel crossing the yield line is orthogonal, and can be in tension only where it is below the neutral axis. Concrete, on

the other hand, is only compressed within the area above the neutral axis, and produces a resultant compressive force normal to the yield line. Individual cross-sections through yield lines are not required to create an equilibrium of normal stresses, except at infinitesimal deflection; each of the flat facets caused by the appearance of discrete yield lines must be in equilibrium under the whole system of resultant forces to which it is subjected. As the deflection increases the neutral axis level rises above the top surface of the slab, leaving only the reinforcement crossing the crack to impose tension in the middle area of the slab. A very similar approach to the kinematics of rectangular slabs in tensile membrane action has recently been used by Herraiz and Vogel [31] in a recent analysis of tensile membrane action of reinforced concrete slabs. Their approach includes an elastic deflection prior to the rigid-plastic yield line phase and assumes that the initial fracture of reinforcement or an estimate of ultimate concrete compressive strain at the slab corners defines structural failure, and they do not consider the behaviour as the reinforcing mesh fractures across yield lines. However, they have modified a bond-slip model based on the FIB Model Code [32] to estimate fracture crack-width. This is clearly worthy of further experimental investigation as an analytical predictor of fracture ductility of the light meshes used in composite slabs.

Wherever the reinforcement in either direction is in tension across a yield line this implies that it is crossing the yield line at a point where there is a separation between the two opposing faces of the discrete crack which defines the extension of a finite length of reinforcing bar as a uniform plastic strain below the fracture strain of the steel material. This finite length depends on failure of the bond between the bar and the concrete over finite lengths either side of the crack. Clearly tensile membrane action would be impossible with perfect bond between steel and concrete, because the bars would fracture instantly within the cracks. On the other hand, remembering that the context in which the behaviour is important is for the relatively thin slabs reinforced only with anti-crack mesh that typically form composite floors, the tensile strength of the steel reinforcement in either direction is less than that of the whole concrete cross-section, and cracking is localized. In more heavily reinforced slabs, in which the reinforcement layer is stronger in tension than the concrete cross-section, the cracking can be distributed over a distance either side of a yield-line. There is currently insufficient reliable information concerning the pull-out characteristics of deformed bars from discrete crack surfaces; this is necessary in order to define the free lengths over which the known fracture strain of the steel bars can be used to specify crack widths at bar fracture. However, significant work has been done in recent years by Cashell et al. [33] and by Sezen and Setzler [34] in developing simplified bond models, either of which could form the basis for a general design model of pull-out at a discrete crack which could be guaranteed as conservative but otherwise accurate. In this paper the problem has been dealt with provisionally for plain welded mesh by assuming that

bars are fully detached from the concrete between the positive “anchor points” at which transverse bars are welded to the bars under consideration (in most practical meshes these are at 200mm spacing, and this has been assumed in the full-scale examples presented), and assigning artificially low ductility to the steel. Essentially, however, this is just one way of defining the crack-width, at the level of the reinforcement, at which a bar fractures, and for the comparisons with model-scale tests on orthotropic slabs experimentally-determined fracture crack-widths have been used, showing an extremely promising degree of correlation with the reducing load capacity in the tests. Clearly there is a need for more work on bar pull-out from discrete cracks, because the fracture of reinforcement across cracks, especially the initiation of “unzipping” of mesh along the diagonal yield lines, has been shown to be the key effect which limits the enhancement of yield-line load capacity with increasing deflection, and initiates structural collapse of the slab. In fire, which will eventually be the context in which this model is most relevant, it should also be capable of including the effect of differential thermal expansions on pull-out characteristics.

It is should be remembered that this work has been done as an essential first step in re-developing a method for assessing the load capacity of lightly-reinforced composite slabs in fire conditions, at very high temperatures which reduce the contribution from the attached steel beams to a very low level. In this context the limiting condition may be either a resistance failure (either local or global loss of structural capacity) of the slab, or as a compartment integrity failure (a through-depth crack which allows flames to pass through to the adjacent compartment at the upper face of the slab). Both of these may be interpreted in different ways. It may be considered that the first peak of capacity in an enhancement curve, often caused by fracture of the bars crossing the central yield line, is sufficient to define a resistance failure, although this usually stabilizes with increasing deflection until a second and final peak is caused by the start of diagonal “unzipping”. The higher of the two peaks definitely indicates the limiting capacity of the slab. In terms of fire compartment integrity there are also different possibilities. The concrete surfaces either side of the central yield line lose contact when the neutral axis depth at the intersections becomes negative; in a composite slab it is likely that steel decking will continue to cross this through-depth crack, creating a physical barrier to hot gases passing through, although there may still be some heat transmission by radiation from the upper surface of this thin sheet. A similar argument may be applied to the appearance of a central through-depth crack across the short span, which initiates a new mechanism not considered in this paper. In either case criteria need to be developed to identify integrity failure of composite slabs.

Subsequent papers will deal with high-temperature applications in which tensile membrane action occurs, as well as explicitly covering the effect of heating of unprotected downstand beams and the reinforcing mesh.

REFERENCES

[1] Johansen, K.W., *"Brudlinieteorier"*, Copenhagen 1943. (English translation *"Yield-Line Theory"*, Cement and Concrete Association, London, 1962).

[2] Hognestad, E., "Yield-line theory for the ultimate flexural strength of reinforced concrete slabs", *ACI Journal*, **49**, March 1953.

[3] Park, R. and Gamble, W., *"Reinforced concrete slabs"*, Wiley, London, 2000.

[4] Ockleston, A. J. "Load tests on a three storey reinforced concrete building in Johannesburg", *The Structural Engineer*, (1955).

[5] Hillerborg, A., "Jamviktsteori for axmerade betongplattor", *Betong,* **41** (4), 1956. (English translation "Theory of equilibrium for reinforced concrete slabs" by G. N. Gibson, Building Research Station Library Communication No. 1082).

[6] Hillerborg, A., *"Strip method of design"*, Viewpoint, London, 1975, 256 pp.

[7] Wood, R.H., and Armer, G.S.T., "The theory of the strip-method for design of slabs", *Proc. ICE*, **40**, (1968).

[8] Park, R., "Tensile membrane behaviour of uniformly loaded rectangular reinforced concrete slabs with fully restrained edges", *Magazine of Concrete Research*, **16** (46), (1964) pp 39-44.

[9] Park R., "Ultimate strength of rectangular concrete slabs under short-term uniform loading with edges restrained against lateral movement", *Proc. Institution of Civil Engineers*, **28**, (1964) pp 125-150.

[10] Brotchie, J.F. and Holley, M.J., *"Membrane action in slabs: cracking, deflection and ultimate load of concrete slab systems"*, Publication SP-30, American Concrete Institute, Detroit, Paper 30-16, (1971) pp 345-377.

[11] Sawczuk, A. and Winnicki, L., "Plastic behavior of simply supported reinforced concrete plates at moderately large deflections", *Int. J. Solids Structures*, **1**, (1965) pp 97-111.

[12] Kemp, K.O., "Yield of a square reinforced concrete slab on simple supports, allowing for membrane forces", *The Structural Engineer*, **45** (7), (1967) pp 235-240.

[13] Hayes, B., "Allowing for membrane action in the plastic analysis of rectangular reinforced concrete slabs", *Magazine of Concrete Research*, **20** (65), (1968) pp 205-212.

[14] Hayes, B., *"A study of the design of reinforced concrete slab structures"*, PhD thesis, University of Manchester, 1968, 398 pp.

[15] Wood, R.H., *"Plastic and elastic design of slabs and plates, with particular reference to reinforced concrete floor slabs"*, Thames and Hudson, London, 1961.

[16] Gillies, A., Unpublished communication

[17] Kirby, B.R., *"The behaviour of multi-storey steel framed buildings in fire: a European joint research programme"*, British Steel Swinden Technology Centre, 1999.

[18] *"BS5950: Structural use of steelwork in buildings: Part 8: Code of practice for fire resistant design"*, British Standards Institution,, London, (1990).

[19] *"ENV1994-1-2: 1992: Eurocode 4: Design of composite steel and concrete structures, Part 1.2: Structural fire design (Draft)"*, European Committee for Standardisation, Brussels, (1992).

[20] Wang, Y.C., "Tensile membrane action in slabs and its application to the Cardington fire tests. Fire, static and dynamic tests of building structures", Proceedings of the Second Cardington Conference, England, (1996), pp 55–67.

[21] Newman G.M., Robinson J.T. and Bailey C.G., *"Fire safe design: A new approach to multi-storey steel-framed buildings"*, The Steel Construction Institute, Ascot, UK (2000).

[22] Bailey, C.G., *"Design of steel structures with composite slabs at the fire limit state"*, BRE Final Report to the Department of the Environment, Transport and Regions, Report No. 81415, Building Research Establishment, Garston, UK, 2000.

[23] Bailey, C.G. and Moore, D.B., "The structural behaviour of steel frames with composite floors slabs subject to fire – Part 1: Theory", *The Structural Engineer*, **78** (11), (2000) pp 19-27.

[24] Bailey, C.G., White, D.S. and Moore, D.B., "The tensile membrane action of unrestrained composite slabs simulated under fire conditions", *Engineering Structures,* **22**, (2000) pp 1583–1595.

[25] Bailey, C.G., "Membrane action of unrestrained lightly reinforced concrete slabs at large displacements', *Engineering Structures*, **23**, (2001) pp 470-483.

[26] Clifton, G.C., *"Design of multi-storey steel framed buildings with unprotected secondary beams or joists for dependable inelastic response in severe fires"*, HERA Steel Design & Construction Bulletin, 60, Manukau City, New Zealand (2001).

[27] Vassart, O. and Zhao, B*., "FRACOF: Fire resistance assessment of partially protected composite floors. Engineering background"*, Arcelor Mittal & CTICM (2011).

[28] Vassart, O. and Zhao, B., *"FRACOF: Fire resistance assessment of partially protected composite floors. Design guide",* Arcelor Mittal & CTICM (2011).

[29] *"BS EN 1992-1-1: 2004: Eurocode 2: Design of concrete structures, Part 1-1: General rules and rules for buildings"*, British Standards Institution, London (2004).

[30] Foster, S.J., Bailey, C.G., Burgess, I.W. and Plank, R.J., "Experimental behaviour of concrete floor slabs at large displacements", *Engineering Structures*, **26** (9), (2004) pp 1231-1247.

[31] Herraiz, B. and Vogel, T., "Novel design approach for the analysis of laterally unrestrained reinforced concrete slabs considering membrane action", *Engineering Structures*, **123**, (2016), pp 313-329.

[32] International Federation for Structural Concrete (FIB). *"fib Model Code 2010, First Edition"*, Ernst & Sohn, Lausanne, Switzerland (2013).

[33] Cashell,K.A., Elghazouli, A.Y. and Izzuddin, B.A., "Experimental and analytical assessment of ductility in lightly reinforced concrete members", *Engineering Structures*, **32** (9), (2010) pp 27292743

[34] Sezen, H. and Setzler, E., "Reinforcement slip in reinforced concrete columns", *ACI Structural Journal*, **105** (3), (2008) pp 280–289.

Notation List

BRE/Bailey method [13, 14, 22, 23]

e	Weighted-mean enhancement factor
e_1, e_2	Enhancement factors for triangular and trapezoidal slab facets
n	Dimensionless coordinate of yield line intersection as a proportion of L (long span)
α	Slab aspect ratio (x:y)
μ	Orthotropy ratio, equivalent to Ω in current method (below)

Current method

A_1, A_{2y}	Concrete stress block areas on diagonal and central yield lines
C	Concrete resultant force across a diagonal yield line
C_{x2}, C_{y2}	Concrete x- or y- direction resultant forces on central yield line
f_{px}, f_{py}	Steel strengths per unit width in x and y directions
f_c	Concrete strength
l	y-dimension of slab
n_x, n_y	Dimensionless coordinates of yield line intersection in x- and y-aligned mechanisms
p	Distributed load intensity on slab
r	Aspect ratio of slab (x:y)
S	Resultant shear force along a diagonal yield line
t	Thickness of slab
T_{x1}, T_{x2}	Tensile resultant forces in x-aligned mesh
T_{y1}, T_{y2}	Tensile resultant forces in y-aligned mesh
u, v	Movements of a point on a crack-face in x and y directions
u_C, v_C	Movements of centroid of diagonal concrete stress block in x and y directions
$u_{T_{x1}}, v_{T_{y1}}, v_{T_{y2}}$	Movements of resultant mesh forces on diagonal and central yield lines
$v_{C_{y2}}$	Movement of centroid of central concrete stress block in y direction
W_e	External work: loss of potential of load on slab
W_i	Internal work: plastic movements of steel and concrete
x, y, z	Coordinate system
$x_{CA,1}, y_{CA,1}, z_{CA,1}$	Coordinates of concrete stress-block centroids on diagonal and central yield lines
$x_{lim,1y}$	Limiting x coordinate of unbroken y-direction reinforcement
$x_{t,1}$	x coordinate at which y reinforcement emerges from compressive stress block
$y_{lim,1x}$	Limiting y coordinate of unbroken x-direction reinforcement
$y_{t,1}$	y coordinate at which x reinforcement emerges from compressive stress block
z_1, z_2	Depths of concrete stress block at slab corner and yield line intersection

γ	Angle of diagonal yield line to y axis
δ_A	Deflection of centre of slab
Δ_x, Δ_y	x and y movements of facets at corner of slab
$\Delta_{lim,x}, \Delta_{lim,y}$	Limiting x and y crack widths at which reinforcement fractures
η_x, η_y	Dimensionless limiting crack widths $\eta_x = \frac{\Delta_{lim,x}}{l}$ and $\eta_y = \frac{\Delta_{lim,y}}{l}$
θ	Rotation of slab Facet 1 about x axis
ϕ	Rotation of slab Facet 2 about y axis
μ	Mesh depth as a proportion of slab thickness
λ_x, λ_y	Dimensionless strength ratios $\lambda_x = \frac{f_{px}}{f_c l}$ and $\lambda_y = \frac{f_{py}}{f_c l}$
ψ_1, ψ_2	Dimensionless stress block depths $\psi_1 = z_1 / l,\ \psi_2 = z_2 / l$
τ	Dimensionless slab thickness t/l
Ω	Orthotropy factor f_{py} / f_{px}

Table Captions

Table 1: Combinations of compression block configuration and rebar fracture for x-aligned cases.

Table 2: In-plane equilibrium equations for different possible x-aligned cases. Cases with concrete stress blocks on central and diagonal yield lines.

Table 3: In-plane equilibrium equations for different possible x-aligned cases. Cases with triangular concrete stress blocks on diagonal yield lines.

Table 4: In-plane equilibrium equations for different possible x-aligned cases. Cases with trapezoidal concrete stress blocks on diagonal yield lines.

Table 5: Combinations of compression block configuration and rebar fracture for y-aligned cases.

Table 6: In-plane equilibrium equations for different possible y-aligned cases. Cases with concrete stress blocks on central and diagonal yield lines.

Table 7: In-plane equilibrium equations for different possible y-aligned cases. Cases with triangular concrete stress blocks on diagonal yield lines.

Table 8: In-plane equilibrium equations for different possible y-aligned cases. Cases with trapezoidal concrete stress blocks on diagonal yield lines.

Figure Captions

Fig. 2: Stages of development of a yield-line mechanism in a concrete slab.

Fig. 3: Illustrations of tensile membrane action. (a) Stresses in a concrete slab; (b) Forces in a bicycle wheel

Fig. 4: Different plastic mechanisms considered by Sawczuk and Winnicki [9].

Fig. 5: Hayes's [10, 11] membrane force models. (a) Concrete contact on whole length of diagonal yield lines; (b) No concrete contact near yield line intersections; (c) In-plane equilibrium of forces.

Fig. 6: Bailey's [10, 11] membrane force model. (a) Concrete contact on whole length of diagonal yield lines; (b) In-plane equilibrium of forces.

Fig. 7: Changes in yield-line geometry for different ratios f_{px}/f_{py}. (a) x-aligned; (b) transition; (c) y-aligned.

Fig. 8: Geometry of diagonal yield-line crack opening. (a) Crack opening at rebar level; (b) Top surface of slab, including rigid-body movements of triangular and trapezoidal slab facets.

Fig. 9: Movements of a point on the diagonal yield line. (a) Plan view of top surface of slab; (b) x-direction motion u on triangular Facet 2; (c) y-direction motion v on trapezoidal Facet 1.

Fig. 10: Projection on the x-direction of the yield lines at different stages; (a) Concrete stress blocks on all yield lines; (b) Triangular stress blocks above rebar on diagonal yield lines; (c) Triangular stress blocks below rebar on diagonal yield lines; (d) Trapezoidal stress blocks on diagonal yield lines.

Fig. 11: The horizontal force system between facets along the yield lines, for x-aligned mechanisms.

Fig. 12: The horizontal force system between facets along the yield lines, for y-aligned mechanisms.

Fig. 13: Slab capacity enhancement factors with displacement for slabs of width 6m and different aspect ratios and mesh effective depths.

Fig. 14: Variation of capacity with aspect ratio for isotropically-reinforced slabs: (a) Dimensionless enhancement factor; (b) Actual capacity for the particular slab cross-section.

Fig. 15: Variation of the resultant forces on yield lines with deflection of the slab (r=1.5, d_l=20mm, ductility 1%).

Fig. 16: Variation of the maximum tensile in-plane bending stresses on yield lines with deflection of the slab (r=1.5, d_l=20mm, ductility 1%).

Fig. 17: Optimal x- and y-aligned yield-line mechanisms for a 9m x 6m slab with mesh effective depth 20mm with different orthotropy ratios; (a) n_x and n_y; (b) Yield-line capacities.

Fig. 18: Enhancement for orthotropic slabs with y-reinforcement constant at 142mm2/m; x-reinforcement areas/m marked in legends. (a) x-aligned mechanisms. (b) y-aligned mechanisms.

Fig. 19: Variation of the maximum tensile in-plane bending stresses at position Q with deflection of the slab (r=1.5, d1=20mm, ductility 1%) for different areas of x-reinforcement per metre, keeping y-reinforcement constant at 141.2mm^2/m.

Fig. 20: Comparison of predicted enhancements according to the new method and BRE with Foster *et al.* tests [30] using smooth reinforcement.

Fig. 21: Comparison of predicted enhancements for different fracture crack-widths according to the new method and BRE with Foster *et al.* tests [30] using deformed reinforcement.